Universidade de Aveiro Departamento de Física
2017

Filipe Mesquita Alves Martinho

Desenvolvimento de Células Solares de Filme Fino de CZTSSe com Inclusão de Selénio nos Precursores

Development of CZTSSe Thin Film Solar Cells with Inclusion of Selenium in the Precursor Stack

Universidade de Aveiro Departamento de Física
2017

Filipe Mesquita Alves Martinho

Desenvolvimento de Células Solares de Filme Fino de CZTSSe com Inclusão de Selénio nos Precursores

Development of CZTSSe Thin Film Solar Cells with Inclusion of Selenium in the Precursor Stack

Dissertação apresentada à Universidade de Aveiro para cumprimento dos requisitos necessários à obtenção do grau de Mestre em Engenharia Física, realizada sob a orientação científica do Doutor António F. da Cunha, Professor Auxiliar do Departamento de Física da Universidade de Aveiro

Ao meu irmão, aos nossos pais e aos nossos avós.

o júri

presidente

Prof. Dr. Leonel Marques Vitorino Joaquim
professor auxiliar do Departamento de Física da Universidade de Aveiro

vogais

Dr. Filipe Carlos Figueiredo Pereira Neves
Laboratório Nacional de Energia e Geologia, IP

Prof. Dr. António Ferreira da Cunha
professor auxiliar do Departamento de Física da Universidade de Aveiro

agradecimentos

Fazer uma dissertação é um trabalho solitário, e muitas vezes ingrato. No entanto, o trabalho de equipa, a troca de ideias e o contacto com áreas de conhecimento diferentes como forma de ganhar novas perspetivas são algumas das armas mais poderosas ao serviço da ciência, e muitas vezes subestimadas ou subvalorizadas. Como tal, gostaria de agradecer aos meus colegas e amigos Bohdan Kulyk e João Lucas Gomes por todas as discussões e sugestões levadas a cabo não só ao longo do último ano, que contribuíram para a melhoria do presente trabalho, mas também durante todos os anos em que vos conheço, que contribuíram para a minha formação como cientista e engenheiro físico. Com vocês aprendi que a ciência se faz aberta e humildemente, em equipa, ao serviço da sociedade e não de interesses próprios.

Doing a dissertation is a lonely work, and often times ungrateful. Nevertheless, team work, sharing of ideas and the contact with other areas of knowledge are some of the most powerful weapons science can have, and are often underestimated or undervalued. As such, I would like to thank my colleagues and friends Bohdan Kulyk and João Lucas Gomes for all the discussions and suggestions given over the course of the last year, which contributed for the improvement of the present work, but also over all the years in which I have known you. With you, I learned that science is done openly and humbly, as a team, for the service of society and not out of self-interest.

palavras-chave

células solares, filmes finos, kesterite, CZTS, CZTSSe, CZTSe, sulfurização, crescimento e caracterização de filmes finos, gradação de composição, gradação de bandgap, formação de bolhas

resumo

Os compostos designados como CZTS (Cu_2ZnSnS_4, $Cu_2ZnSnSe_4$ e $Cu_2ZnSn(S_x, Se_{1-x})_4$) constituem atualmente uma das maiores promessas para produção de células solar à escala de TW, devido ao uso de elementos abundantes e ambientalmente benignos, ao contrário dos compostos equivalentes no sistema CIGS. Contudo, ainda é necessário ultrapassar algumas barreiras de modo a atingir níveis de performance necessários para o desenvolvimento à escala industrial desta tecnologia.

Uma tendência de investigação promissora consiste em introduzir uma gradação vertical no *bandgap*, ao longo da espessura da camada absorvente, através da variação do rácio $S/(S+Se)$.

Neste trabalho, camadas absorventes à base de $CZTS_xSe_{1-x}$ foram produzidas pelo método de deposição de precursores empilhados por pulverização catódica seguido de sulfurização em H_2S, em que o elemento Se é introduzido nos precursores por evaporação térmica. Duas configurações foram testadas: uma com a sequência de empilhamento $ZnS/SnS_2/Se/Cu$ repetida por vários períodos, e outra em que uma única camada de Se é introduzida no topo da sequência total de precursores. Usando este método, foram atingidos rácios $S/(S+Se)$ aproximados desde 1 até perto de 0.5. A gradação da composição em profundidade foi parcialmente atingida, como é revelado através de *Radio-frequency Pulsed Glow Discharge Time-of-Flight Mass Spectrometry* (rf-PGD-TOFMS).

As camadas absorventes resultantes foram usadas para fabricar células com a estrutura $SLG/Mo/CZTSSe/CdS/i\text{-}ZnO/ITO$. A eficiência máxima atingida nos dispositivos fabricados foi 1.3%, numa camada com um rácio $S/(S+Se)$ aproximado de 0.91, produzida a partir de precursores com Se no interior dos precursores empilhados. Microscopia de Eletrões Secundários (SEM), Espetroscopia de Dispersão de Energia (EDS), espetroscopia Raman e rf-PGD-TOFMS foram usados para caraterizar as amostras produzidas.

As camadas absorventes produzidas, incluindo as com maior eficiência fotovoltaica, exibiram bolhas, rebentadas ou não rebentadas, e que rebentavam superficialmente ou rebentavam expondo o contacto inferior completamente, dependendo das condições de processamento. Este fenómeno foi estudado em detalhe, e novas observações não reportadas na literatura até ao momento foram encontradas, apontando para a possibilidade de controlar a formação de bolhas através do ajuste do perfil de sulfurização. Baseado nestes resultados, sugere-se uma revisão dos modelos propostos na literatura, e propõe-se um novo modelo baseado na volatilização de reagentes.

keywords

solar cells, thin films, kesterite, CZTS, CZTSSe, CZTSe, sulfurization, growth and characterization of thin films, composition grading, bandgap grading, blister formation

abstract

CZTS-based compounds (Cu_2ZnSnS_4, $Cu_2ZnSnSe_4$ and $Cu_2ZnSn(S_x, Se_{1-x})_4$) have become one of the major contenders for solar cell production at the TW level owing to the use of earth-abundant and environmentally benign elements, unlike their CIGS counterparts. However, some hurdles still need to be overcome in order to achieve performance levels necessary for industrial scalability. One promising trend of investigation consists in introducing a vertical bandgap grading along the thickness of the absorber by means of a variation of the $S/(S + Se)$ ratio.

In this work, $CZTS_xSe_{1-x}$ absorbers were produced by the standard two-step process of sputtering deposition of a precursor stack followed by annealing in H_2S, where the element Se was added in the precursor deposition stage using thermal evaporation. Two configurations were tested: one with the stacking sequence $ZnS/SnS_2/Se/Cu$ repeated for various periods, and another configuration where a single Se layer is evaporated on top of the multi-period precursor stack. Using this method, average $S/(S + Se)$ ratios from 1 to close to 0.5 were demonstrated. Composition grading in depth was partially achieved as shown by Radiofrequency Pulsed Glow Discharge Time-of-Flight Mass Spectrometry (rf-PGD-TOFMS).

The resulting absorbers were used to fabricate solar cells with the structure $SLG/Mo/CZTSSe/CdS/i\text{-}ZnO/ITO$. The highest efficiency achieved in the devices produced was 1.3%, using an absorber with an average $S/(S + Se)$ of 0.91, produced from precursors with Se within the stack. Secondary Electron Microscopy (SEM), Energy Dispersive Spectroscopy (EDS), Raman spectroscopy and rf-PGD-TOFMS was used to characterize the absorbers produced.

The absorbers produced, including the highest performing devices, exhibited blisters, which would either burst or not burst, and burst either superficially or completely exposing the back contact, depending on processing conditions. This phenomenon was studied in detail, and new evidence was found, which has not been considered in literature so far, pointing to the possibility of significantly controlling blister formation by appropriately tuning the sulfurization profile. Based on these results, a review of the models proposed in literature to explain blister formation in CZTS is suggested, and a new model based on the volatilization of reactants is proposed.

Contents

1. Introduction

1.1. The rise of solar photovoltaics: Swanson's law and grid parity

The field of solar photovoltaics (PV) has experienced a remarkable growth over the past few years, and the solar PV penetration rates in the energy markets will increase even further – with both the United States and the European Union having already committed to achieving an energy mix with at least 30 % of energy from renewable sources by 2030, several reports state that solar PV is expected to comprise as high as 15 % of the whole global energy market by that year [1], [2]. Such an increase is made possible mainly due to a significant reduction in the operational and production costs of the PV technologies. One of the relevant metrics used to characterize this reduction is the PV learning curve, also known as Swanson's Law[1], analogous to Moore's law in electronics [3]. Swanson's law results from the empirical observation that the cost of solar PV has been systematically decreasing at a rate of over 20 % every time the production doubles. This tendency, illustrated in Fig. 1.1, is based on data collected since 1976, and has even increased to 39 % considering only the period from 2006 to 2016, making an overall learning rate of about 22.5 % [1].

This price reduction tendency has made the energy from solar PV increasingly more cost-competitive in comparison with conventional non-renewable sources, and in some cases the cost of solar PV energy already matches that of these sources, a condition where it is then said that solar PV (or any other alternative energy source) has achieved "grid parity". In a recent report by the

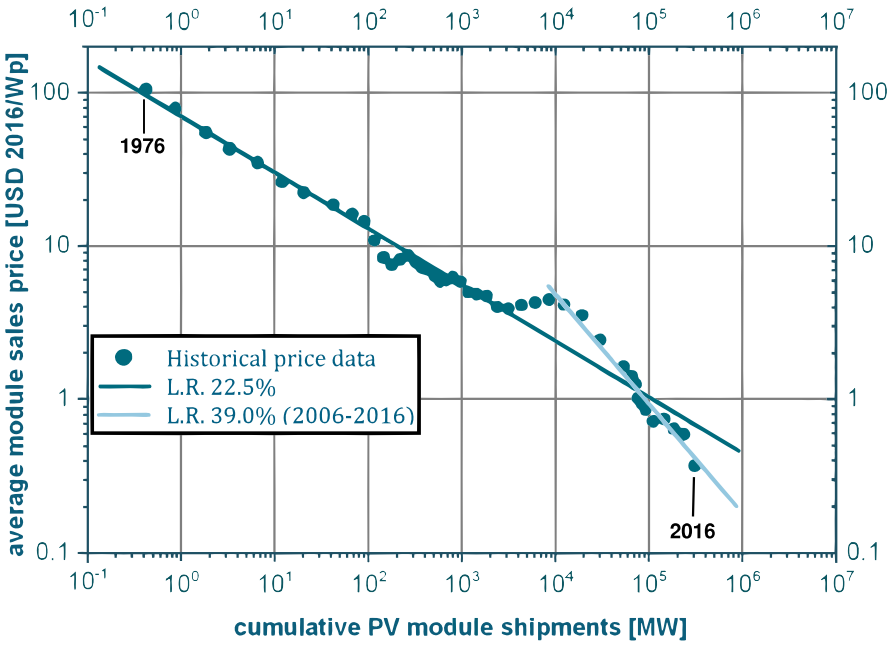

Fig. 1.1 – Swanson's Law: learning rates (L.R.) in the PV industry for the average cost of solar modules as a function of cumulative module shipments. The percentages correspond to a cost reduction after a doubling in shipment volumes. Each dot corresponds to a year. Adapted from [1].

[1] Named after Richard Swanson, the founder of the solar manufacturer *SunPower Corporation*.

Deutsche Bank [4], out of a sample of over 60 countries analyzed, it was estimated that roughly 30 of them had already achieved grid parity for solar PV in 2015, either on residential or utility scale. In 2016, solar PV energy was negotiated at unprecedented prices in some countries, already beyond grid parity equilibrium. In the United Arab Emirates, several solar PV projects were negotiated under 0.0280€/kWh, with an absolute record of 0.0227€/kWh in Abu Dhabi [1], [5]. A contract for a 120 MW solar PV plant was won at 0.0273€/kWh in Chile[2] [5]. As an example for comparison, in the Iberian wholesale energy market (for Portugal and Spain), where solar PV is estimated to be also already at grid parity, the average cost of the energy negotiated in 2016 was slightly under 0.04 €/kWh [6]. This energy was then distributed to retail customers at prices ranging roughly from 0.1 to 0.3 €/kWh in Portugal [7].

1.2. A market ruled by Silicon and the need for additional research

The evolution described in the previous section was based on crystalline silicon solar cells (c-Si), which have been dominating the solar PV market, systematically accounting for 80 - 95 % of module shipments for decades [8]. However, other solar cell technologies have managed to enter the market, and with manufacturing and overall costs already on par with those of c-Si: CdTe- and CIGS-based solar cells, as shown in Fig. 1.2.

The success of CdTe and CIGS (abbreviated from $Cu(In,Ga)(S,Se)_2$) cells comes from their

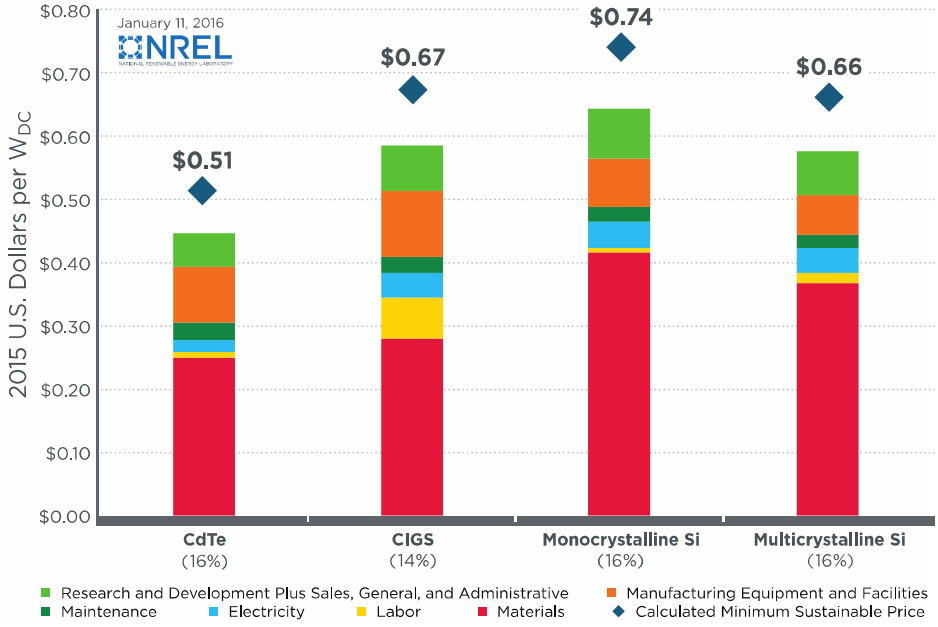

Fig. 1.2 – Cost estimates for the several solar cell technologies in 2015. The average module efficiencies are shown in parenthesis. Adapted from [8]. Notice that the estimated costs are consistent with those of Fig. 1.1 for 2015.

[2] Converted from U.S. Dollars with the rate 1 US$ = 0.9375 €

ability to match the efficiency of c-Si cells with a significant reduction in material costs, as shown in Fig. 1.2. Despite the significant reduction in Si wafer prices in recent years [1], materials cost still accounts for the majority of the cost of a c-Si cell, which is one of the sources of criticism directed towards this technology. In contrast, CdTe and CIGS cells cut costs by making use of materials with a direct bandgap (unlike Si), achieving absorption coefficients above 10^4 cm^{-1} for sunlight, which allows the use of absorber layers around 1 μm thick, 2 orders of magnitude thinner than c-Si absorbers. These thinner cells are thus named thin film solar cells, and it is believed that thin film solar cells are the most cost-effective route to fabricate solar cells. Beyond this cost reduction paradigm, the use of thinner layers also allows the fabrication of cells on flexible substrates, which opens a new world of applications not possible with c-Si cells [9].

Despite their success, both CdTe and CIGS cells have shortcomings which hinder them from increasing their market share. The elements Cd and Te are hazardous substances, under a strict control by EU directives [10], raising concerns on the life cycle waste management and its impact on costs. The elements Te and In are rare, with concentrations in the continental crust of 0.001 and 0.05 ppm respectively [11]. The scarcity of In and Te is estimated to bottleneck the production of CIGS and CdTe solar cells at around 70 GW/year and 2.3 GW/year, respectively, which is an insufficient rate to quickly achieve TW levels [12], [13]. These problems highlight the relevance of research in alternative non-toxic and abundant materials for solar cells. There are several new solar cell technologies showing promising results and attracting increasing attention, such as organic/hybrid, quantum dot, perovskite and other inorganic thin film solar cells alternative to CdTe and CIGS.

1.3. CZTS thin film solar cells as a promising candidate for TW production

One alternative which has attracted a lot of interest recently replaces In and Ga in CIGS by the earth-abundant metals Zn and Sn, and uses either Se or S. This results in a family of compounds generally labeled as CZTS – $Cu_2ZnSnSe_4$ (CZTSe), Cu_2ZnSnS_4 (CZTS, or pure-CZTS to avoid ambiguity) and $Cu_2ZnSn(S_xSe_{1-x})_4$ (CZTSSe). The abundance of Cu, Zn and Sn in the continental crust is 25, 71 and 5.5 ppm, respectively [11], and with the exception of Se, all its elements are nontoxic, making CZTS a potential candidate for TW production using only a fraction of the annual production of its elements [9].

Due to their isovalency and similar crystal structure, the CZTS system preserves the favorable characteristics of CIGS for PV applications. It offers a high absorption coefficient of over 10^4 cm^{-1} and a tunable optical bandgap from 1.0 to 1.5 eV, allowing an optimization of sunlight absorption [14], which will be further discussed in the next sections. However, the efficiency of CZTS-based solar cells has yet to match the efficiencies of CdTe and CIGS cells, whose current

records are set at 22.1 % and 22.3 %, respectively (see [15] and references therein). A promising record efficiency of 12.6 % for CZTSSe was obtained in late 2013 via non-vacuum solution processing methods [16], and matched in 2016 using vacuum-based methods, which yielded a 12.3 % efficient cell [17]. Some of the challenges required to overcome this performance gap between state of the art CIGS and CZTS solar cells will be discussed in this work.

1.4. The scope of this work

The promising prospects of CZTS-based solar cells are attracting considerable attention from researchers and, according to the *Scopus* database, there are already more than 2000 papers published in the field, with a growth of around 400 papers/year registered in 2015 and 2016. There are already dozens of review articles providing detailed information on the properties of the CZTS system, both experimental and from theoretical simulations, including (but not limited to) crystal structure studies, the phase diagram and secondary phases of the CZTS system, reaction chemistry and thermodynamics, defect physics, defect passivation strategies, grain boundaries, electric and transport properties, electronic density of states, band structure, optical and optoelectronic properties, fabrication steps and strategies, and relevant characterization methods. Furthermore, a number of papers have focused on specific aspects of the architecture of CZTS cells, namely the back-contact/CZTS and CZTS/buffer interfaces, with the latter being currently one of the hottest topics in the field, as researchers try to find buffer layers alternative to CdS. One should see, for example, the recent reviews by Liu *et al*. [18] which also refers to 19 other review articles, and by Gershon *et al* [19]. There is also already a book exclusively dedicated to CZTS-based solar cells, by Kentaro Ito [9], which compiles a lot of information in a detailed and comprehensive way.

Given the extent of information available on CZTS and the short nature of the present work, doing an extensive literature review would render it irrelevant. Instead, some selected key topics will be discussed, and used to complement the practical work conducted whenever possible.

The present work attempts to produce CZTSSe-based solar cells, focusing on the optimization of the absorber layer's production methods, through a series of iterative steps based on information collected from several characterization techniques. In addition, the ensuing discussions will feature numerical simulations, to complement them and highlight the relevance of the chosen approaches. The simulations will be based on the *SCAPS* software.

2. The SCAPS software – short description

The SCAPS software – Solar Cell Capacitance Simulator – was created by researchers at the university of Gent (Belgium) [20]. It was originally developed to simulate the behavior of CIGS and CdTe cells, and was then extended to other thin film solar cells such as CZTS, and to some

other types of solar cells. Its main functionality is to numerically solve the one-dimensional semiconductor equations governing the behavior of the devices. In the bulk, these equations are [20]:

Poisson equation

$$\frac{\partial}{\partial x}\left(\varepsilon_r \frac{\partial \psi}{\partial x}\right) = -\frac{q}{\varepsilon_0}\left[p - n + N_D^+ - N_A^- + \frac{1}{q}\rho_{defect}(n,p)\right] \quad (1)$$

Continuity equations

$$\frac{\partial n}{\partial t} = G - U_n - \frac{\partial j_n}{\partial x} \quad (2)$$

$$\frac{\partial p}{\partial t} = G - U_p - \frac{\partial j_p}{\partial x} \quad (3)$$

Constitutive equations

$$j_n = -\frac{\mu_n n}{q}\frac{\partial E_{Fn}}{\partial x} \quad (4)$$

$$j_p = \frac{\mu_p p}{q}\frac{\partial E_{Fp}}{\partial x} \quad (5)$$

where ε_r and ε_0 are the relative and vacuum permittivity, respectively, ψ is the electrostatic potential, q is the elementary charge, n and p are the electron and hole carrier densities, respectively, N_A^- and N_D^+ are the shallow charge acceptor and donor densities, respectively, ρ_{defect} is a function that describes the density of defects, G is the carrier generation rate, $U_{n,p}$ are the recombination rates, $j_{n,p}$ are the carrier fluxes (such that $qj_{n,p} = J_{n,p}$, the traditional current densities), $\mu_{n,p}$ are the mobilities, respectively, and finally $E_{Fn,p}$ are the quasi-Fermi energies. The system is then complete with the appropriate boundary conditions for each interface and contact defined by the user. SCAPS solves these equations for (ψ, n, p) or $\left(\psi, E_{Fn}, E_{Fp}\right)$ by discretizing each layer into a mesh using finite differences, and then applying a Gummel iteration scheme with Newton-Raphson substeps (see references in [20]).

In this work, a standard Mo/CZTSSe/CdS/ZnO/ITO solar cell model was constructed in SCAPS, by gathering information on its properties and behavior from literature. Many properties were scattered across different publications, so a complete list of the sources consulted will not be provided, for the sake of brevity[3]. The main sources, where the reader will find most of the necessary parameters, are [9], [21]–[25], with the last three focusing specifically in ZnO and ITO. More information on certain modeling details will be provided in the sections where it is used.

[3] For a more in depth description of the model used please contact the author of this work.

3. Brief analysis of the CZTS solar cell architecture: selected topics

Much of the early success of CZTS-based solar cells was achieved by simply copying both the architecture and production methods which achieved the best results in CIGS, and from then on several incremental innovations were introduced. The architecture which is by far the most used, and serves as benchmark for both CZTS and CIGS cells, is depicted in Fig. 3.1 (a). It has the structure BC/Absorber/Buffer/Window/FC, where BC and FC are the back and front contacts (relative to light incidence), using Mo/CZTS/CdS/TCOs [9], where TCOs are the transparent conductive oxides, usually ITO (Sn: In_2O_3), FTO (F: SnO_2) and AZO (Al: ZnO) [24]. The corresponding band diagram at zero bias, which will serve as basis for the discussion in the next sections, is shown in Fig. 3.1 (b). The p-CZTS/n-CdS heterojunction provides the built-in field for charge separation. Besides forming the pn junction, the CdS layer shields the absorber from being damaged during the production of the window layers, and is thus labeled buffer layer [9].

In general, window layers can serve multiple purposes. Their use greatly decreases the surface recombination velocity of the cell when compared to a simple Absorber/FC configuration. They can also passivate surface defects of the preceding layer, and provide a resistive pathway to shunts within the device. In order to avoid light absorption losses, these layers are made very thin and use materials with a high bandgap, making them nearly transparent to visible light. For this reason, they are called window layers[4] [9], [27]. In addition to the optimization of the properties of the absorber itself, the BC/CZTS and CZTS/Buffer interfaces are considered to be crucial for the improvement of the performance of the cell, and have been central topics of discussion among researchers. These will be further detailed in the next sections.

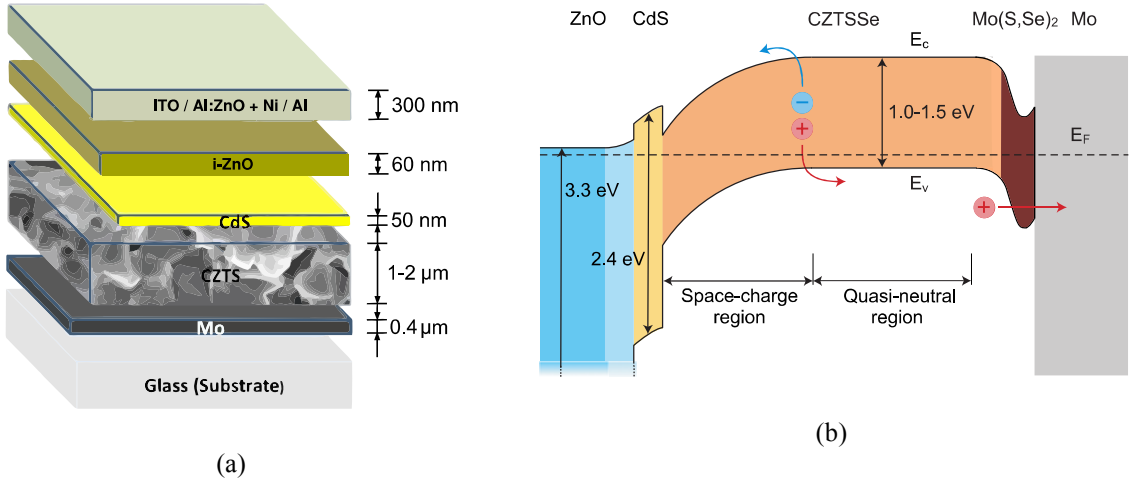

Fig. 3.1 – (a) Benchmark architecture of a CZTS solar cell and typical thicknesses as used in this work. Adapted from [14]; (b) Typical simplified zero bias band diagram of the CZTS benchmark architecture. Adapted from [26].

[4] Notice that due to its high bandgap of 2.4 eV, CdS is also a window layer. It is therefore commonly referred to both as a window and as a buffer layer in literature.

3.1. The Mo/CZTS interface

The use of Molybdenum as BC for hole collection was very successful in CIGS cells. It has a high conductivity, it can withstand high processing temperatures of up to 650 °C and it allows the diffusion of sodium into the absorber (e.g., when a glass substrate is used), which was shown to improve the properties of both CIGS and CZTS absorbers [28], [29]. Furthermore, Mo reacts with both the absorbers during thermal processing, forming a $\mathrm{Mo(S,Se)_2}$ compound, an intrinsically n-type semiconductor. In CIGS, this compound was found to be highly beneficial as it forms a nearly ohmic contact with Mo, which was ascribed, using direct and inverse photoemission studies, to a favorable valence band alignment and to an upward band bending due to an n-$\mathrm{Mo(S,Se)_2}$/Mo Schottky contact that facilitates hole transport towards the BC [30]. In CZTS, however, some detrimental effects appear to come up with the use of Mo as BC. While forming the $\mathrm{Mo(S,Se)_2}$ compound, both CZTS and CZTSe appear to decompose at the typical processing temperatures of 500 - 600 °C, which can be described by reaction (6) [31]:

$$\mathrm{2Cu_2ZnSnS(e)_4 + Mo \rightleftharpoons 2Cu_2S(e) + 2ZnS(e) + 2SnS(e) + MoS(e)_2} \qquad (6)$$

Reaction (6) was calculated to lead to a variation in Gibbs free energy of -100 kJ for CZTSe and -150 kJ for CZTS at 550 °C, meaning that the decomposition is thermodynamically favorable. Moreover, this reaction was found to occur at a fast rate, with thicknesses of $\mathrm{Mo(S,Se)_2}$ of 20 and 60 nm seen after 3 and 30 min of annealing in an inert atmosphere, respectively [31]. On the other hand, the decomposition of CZTS(e) in its so-called secondary phases and their individual impact on device performance is well-documented (for instance see [9], [14]). In order to circumvent this problem, two general approaches are being followed: (i) implementing a different BC or (ii) preventing reaction (6) from occurring, for example by controlling specific process parameters or by introducing other functional layers between CZTS and Mo. Promising results have been achieved, with device efficiencies over 10%. For further discussion, see [14], [18], [32].

The behavior of the Mo/CZTS interface is, however, still not fully understood. For instance, a nearly 200 nm thick $\mathrm{Mo(S,Se)_2}$ was reported in the highest-performing CZTSSe solar cells produced thus far, and a thickness of over 300 nm was also reported in several other state-of-the-art devices [16], [33]. Yet several reports in literature suggest that the formation of $\mathrm{Mo(S,Se)_2}$ and corresponding decomposition of CZTS could correlate with the creation of voids and defects at the Mo/CZTS interface, leading to a high series resistance and low open circuit voltage V_{oc}, low fill factor FF and low short circuit current density J_{sc} of devices [14], [18]. This gives rise to a somewhat confusing situation where some authors suggest a change in the BC configuration [31] while others do not consider the Mo/CZTS interface a relevant problem at all [34]. One hypothesis which has been presented speculates that annealing in a sulfur containing atmosphere (which is widely

employed in CZTS thermal processing) could reduce the rate of decomposition of reaction (6) by means of a concomitant recovery reaction, which might mask the shortcomings of the Mo BC, but cannot stop it altogether (see the discussion in [31]). As far as it could be determined from the analysis of recent literature, this hypothesis seems to be backed up by other findings, such as the observation that by adding SnS powders during thermal processing both the formation of the $\mathrm{Mo(S,Se)_2}$ layer and the decomposition of CZTS can be hindered [35], [36].

The previous discussion highlights the need for further work to clarify these issues, which is scarce at the moment when compared to other aspects of CZTS-based cells. This is in part because it is difficult to study the BC/Absorber interface properly, whether in CZTS or in CIGS, since it forms during the processing of the absorber and is only finished once the absorber itself is finished, being affected by multiple parameters – some of which were described in the previous paragraph for the case of CZTS [30]. Two different studies, conducted using different characterization methods, found evidence that a hole-blocking barrier can indeed be present at the Mo/CZTS interface [30], [37]. In particular, by analyzing the $\mathrm{Mo/MoS_2/pure\text{-}CZTS}$ contact properties using photoemission studies (XPS and UPS), it was determined that the $\mathrm{MoS_2}$ bands bend upwards towards Mo, which would not constitute a barrier for hole extraction. The problem, then, seems to lie on the $\mathrm{MoS_2/CZTS}$ side [38], where a hole-blocking potential barrier can be found. This information was used to purposefully redraw the band diagram near the BC, shown in Fig. 3.1 (b). The band offsets were neglected for the sake of simplicity.

It would then be pertinent to ask – what would happen if we could somehow completely suppress the formation of the $\mathrm{Mo(S,Se)_2}$ layer? Would Mo be an adequate contact for CZTS then? Although the answer is far from simple, let's start by analyzing it according to the classical theory of Bardeen for metal-semiconductor contacts [39]. In the simplest case possible, where the interface states are negligible, and in equilibrium, the potential barrier Φ_{Bp} for hole injection from the metal to the semiconductor would be given by Schottky-Motts's rule [40, Ch. 3]:

$$q\Phi_{Bp} = E_g - (\phi_m - \chi_s) \tag{7}$$

where E_g is the bandgap energy, ϕ_m is the metal work function and χ_s is the semiconductor electron affinity. Note, however, that we are interested in the extraction of holes from the semiconductor to the metal instead, which has an energy barrier just short of $q\Phi_{Bp}$ by the difference between the Fermi energy E_F and the valence band energy E_v in the semiconductor. The corresponding voltage is the built-in voltage V_{bi} of the contact, which can also be written as $qV_{bi} = \phi_m - \phi_s$, where ϕ_s is the semiconductor work function [40, Ch. 3]. The presence of this barrier is detrimental since it leads to a voltage drop across the contact, which lowers the V_{oc} and efficiency η of

devices. This discussion can be illustrated using a very simple exercise. Consider an ideal Mo/pure-CZTS/CdS/ZnO/ITO solar cell, where no intentional detrimental effects (e.g. non-radiative recombination in added defect centers) are introduced. The effect of the variation of the Mo BC work function on the cell's IV curve is simulated for this system using SCAPS, taking into account that the reported ϕ_{Mo} ranges from around 4.4 to 5.0 eV [41]. The results, shown in Fig. 3.2, reveal that the change of ϕ_{Mo} significantly affects the device performance. By increasing ϕ_{Mo}, the hole extraction barrier decreases, improving the V_{oc} of devices. The flat-band condition corresponds to a perfectly ohmic contact, where no barrier would occur. The corresponding high performance is simply the Shockley-Queisser (SQ) limit for an ideal pn junction solar cell with an absorber bandgap of 1.5 eV [42].

If the Schottky-Mott model was an accurate description of the Mo/CZTS interface, the results of Fig. 3.2 would immediately show that its work function is too low, and it would be far more beneficial for there to be an intermediate $\mathrm{Mo(S,Se)_2}$ layer, as real devices subject to non-ideal conditions already perform at the level shown in this simulation. If, instead, we consider the influence of interface states, Bardeen's model predicts that Φ_{Bp} would be in the form [40, Ch. 3]:

$$q\Phi_{Bp} = E_g - (c_1\phi_m + c_2) \tag{8}$$

where c_1 and c_2 are constants specific to the chosen semiconductor. For the more well-known semiconductors such as Si these constants are well-known and the results agree reasonably with the model of Eq. (8) for a plethora of metals (see references in [40, Ch. 3]). However, for semiconductors used in thin film solar cells such as CZTS, no such studies have been conducted so far. It

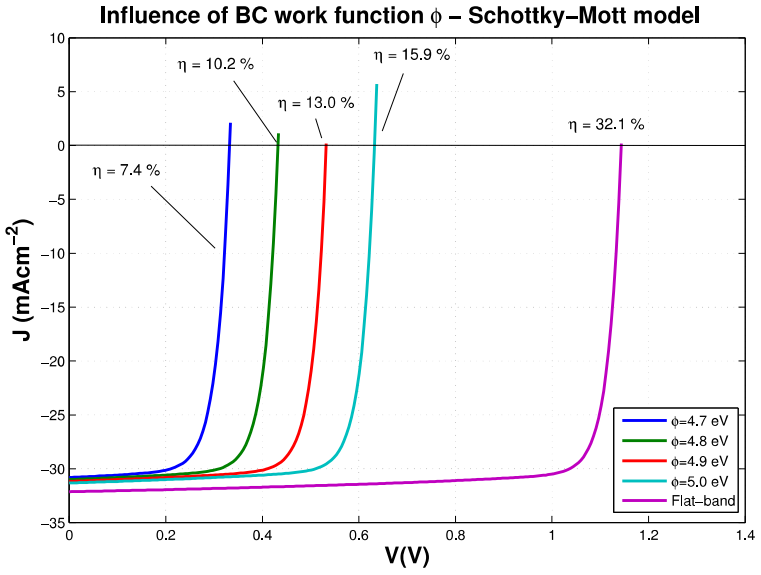

Fig. 3.2 – SCAPS simulation of the light IV curve variation for the benchmark CZTS cell by changing the Molybdenum work function. The "flat-band" condition artificially removes any hole collection barrier in the interface.

should also be noted that in the limit where the number of interface states becomes very large, the barrier heights become independent of the metal work function – a condition known as Fermi level pinning – and are exclusively determined by the semiconductor surface properties. This condition is unfavorable as it makes it harder to form ohmic contacts [40, Ch. 3].

The previous discussion becomes even more complex, as Bardeen's theory does not consider other relevant effects such as metal-induced gap states, which can further pin the Fermi level, and the occurrence of chemical reactions at the interface – as has been discussed for the case of Mo in CZTS, where the effects of the formation of $\mathrm{Mo(S,Se)_2}$ are still relatively unknown [21]. Modern theory shows that the physics and chemistry of Schottky barrier formation should be assessed individually for each contact by means of a quantum mechanics-based approach [43]. As CZTS is becoming a relevant semiconductor in the field of photovoltaics, such a study might be in order.

3.2. The absorber layer

3.2.1. Phase stability, defects and composition control

One of the difficulties which has been identified in achieving highly efficient devices is the narrow phase stability of CZTS compounds. Studies have shown that the region of phase stability of CZTS, illustrated in Fig. 3.3 for the pure sulfide compound, is narrower than in the case of CIGS [44]. The practical implications of this result are that a more rigorous control of production parameters is needed in order to avoid the presence of secondary phases and, at the same time, adequate etching methods need to be implemented in order to remove any unwanted phases.

It has been empirically determined that the efficiencies of devices are highest when the absorber composition is slightly Cu-poor and Zn-rich, with the ideal elemental ratios of [45]:

$$\frac{\mathrm{Cu}}{\mathrm{Zn}+\mathrm{Sn}} \sim 0.7\text{-}0.9 \text{ and } \frac{\mathrm{Zn}}{\mathrm{Sn}} \sim 1.0\text{-}1.3 \tag{9}$$

This optimal composition region is illustrated as the bigger circle in Fig. 3.3. Notice that this region is slightly deviated from the stable region of CZTS, and calculations do show that under Cu-poor conditions the stable region of pure-CZTS becomes even narrower. It is thus expected that several secondary phases can coexist with CZTS under the conditions in (9). These results can be extended to the case of CZTSe, as their phase diagrams are very similar [44], [45].

The most stable crystal structure for CZTS compounds was found to be the kesterite structure, which in the Hermann-Maugin notation corresponds to the I-4 (or $I\bar{4}$) space group [47]. The kesterite structure is depicted in Fig. 3.4 (a) for pure-CZTS. However, a partial structural disorder is expected to occur, due to the complex intrinsic defect physics that typically arises in quaternary compounds. The effects of the kesterite stability and structural disorder on photovoltaic performance are currently still under investigation (for example [34], [47]). The defect physics of CZTS compounds contains a series of vacancy, interstitial and antisite defects. The ionization levels of some of these defects in the bandgap of pure-CZTS are shown in Fig. 3.4 (b). The results from Fig. 3.4 (b) show that the V_{Cu} vacancy and Cu_{Zn} antisite are the shallowest acceptor defects. Additionally, according to theoretical work, they have the lowest formation energy among all the known de-

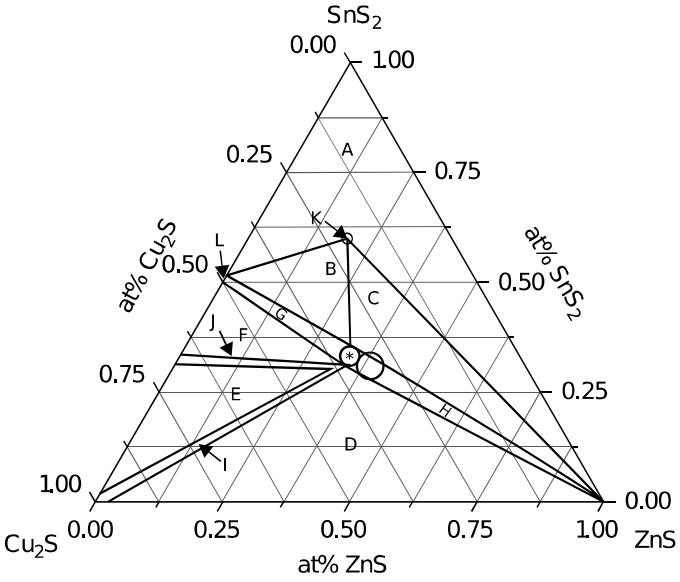

Fig. 3.3– The phase diagram for the Cu-Zn-Sn-S system at 400 °C. Adapted from [9], based on experimental results from [46]. The symbols describe the formation regions of the different phases:
$* - Cu_2ZnSnS_4 = \alpha$
$A - \beta + SnS_2 + Cu_2SnS_3 + ZnS$
$B - \alpha + Cu_2$
$C - \alpha + ZnS + \beta$
$D - \alpha + Cu_2S + ZnS$
$E - \alpha + Cu_4SnS_4 + Cu_2S$
$F - \alpha + Cu_4SnS_4 + Cu_2SnS_3$
$G - \alpha + Cu_2SnS_3$
$H - \alpha + ZnS$
$I - \alpha + Cu_2S$
$J - \alpha + Cu_4SnS_4$
$K - Cu_2ZnSn_3S_8 = \beta$
$L - Cu_2SnS_3$
The bigger circle marks the region of optimal composition, given by (9).

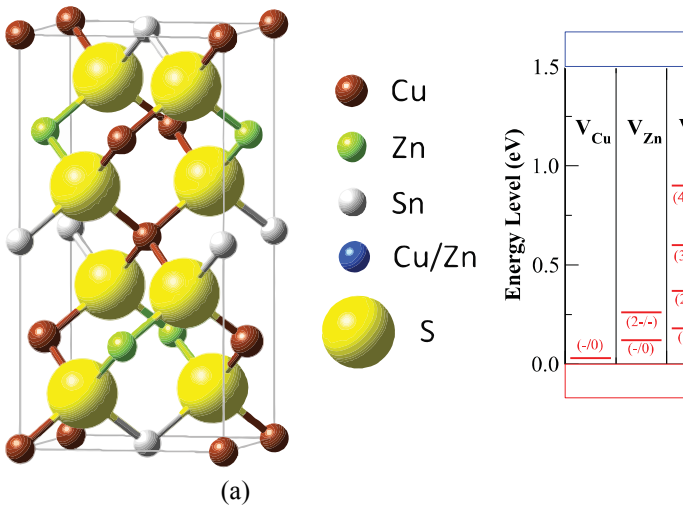

(a)

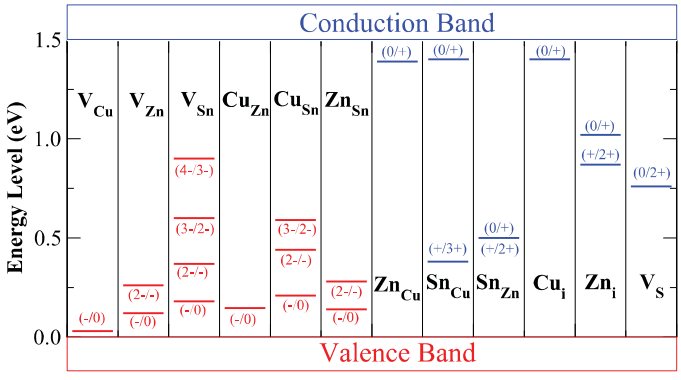

(b)

Fig. 3.4 – (a) The kesterite crystal structure of CZTS compounds. Adapted from [34]; (b) Ionization levels of single intrinsic defects of pure-CZTS, with acceptors in red and donors in blue. After [44].

fects. Thus, at least one of these two defects is expected to be present in high concentrations, both in CZTS and CZTSe, which explains the intrinsic p-type conductivity of these compounds [44].

The discussion in the previous paragraph is, nevertheless, overly simplistic. The single defects referred in Fig. 3.4 can appear in spatial proximity, giving rise to defect clusters which exhibit different properties. In fact, it is believed that the cation ratios described by (9) could lead to a decrease in the density of certain detrimental defect clusters – such as $[2\mathrm{Cu_{Zn}} + \mathrm{Sn_{Zn}}]$, which can enhance either electron-trapping or recombination –, and favor the production of more benign or even beneficial ones instead – the case of $[\mathrm{Zn_{Sn}} + 2\mathrm{Zn_{Cu}}]$ and $[\mathrm{V_{Cu}} + \mathrm{Zn_{Cu}}]$, respectively [9], [44], [45]. Defect engineering through composition control thus plays a major role in improving the properties of the absorber layer.

3.2.2. Bandgap grading as a possible optimization

In the search for ways to improve the efficiency of CZTS cells, one promising method that has recently been tried consists in introducing a bandgap grading in the absorber layer [17]. When properly implemented, this has already been shown to improve the performance of CIGS cells [26]. In its simplest form, a bandgap gradient is introduced along a certain thickness of the cell. This creates an additional electric field component which promotes the separation of generated carriers and prevents them from diffusing to the wrong contact and recombining. Additionally, it tunes the absorption to different photon energies, increasing the amount of generated carriers, which increases J_{sc}. In the case of CIGS, this grading has been described to occur mainly on the conduction band, with the valence band being approximately constant [48][5]. There, a favorable grading would be for the bandgap to decrease from the back to the front, which is known as normal grading. Another reported configuration incorporates both this previous grading and a counter-grading with the bandgap increasing near the heterojunction interface, thus creating a double grading [48]. The idea behind this inclusion is to achieve a high J_{sc} without a loss in V_{oc} – which would otherwise occur, as J_{sc} and V_{oc} are a natural trade-off in photovoltaics – by avoiding a bandgap narrowing near the heterojunction interface. However, this double grading should not be too pronounced, to avoid creating a notch in the conduction band that would trap electrons and increase recombination [26].

In CZTS-based cells, such gradings are possible by changing the $\mathrm{S}/(\mathrm{S}+\mathrm{Se})$ ratio. This changes the bandgap of $\mathrm{Cu_2ZnSn(S_xSe_{1-x})_4}$ according to

$$E_g(x) = xE_g(CZTS) + (1-x)E_g(CZTSe) + x(1-x)b \tag{10}$$

[5] An approximation in a rather complex topic. It seems to be more accurate for In/Ga grading, but for S/Se grading changes do occur in the valence band. See for example the discussion in other simulation papers [53], [82].

where $\mathrm{E_g(CTZS)}\sim 1.5$ eV, $\mathrm{E_g(CTZSe)}\sim 1.0$ eV and b is the bowing factor, which has been reported to be between -0.19 and 0.08 eV [9]. The value $\mathrm{b} = -0.07$ eV was chosen for this work, in accordance with reference [49].

In order to illustrate the potential effects of bandgap grading in CTZS, another example of modeling using SCAPS is devised. An ideal $\mathrm{Mo/CZTSSe/CdS/ZnO/ITO}$ cell is first considered, where a bandgap variation according to (10) is introduced, assuming that only the conduction band position is changed. The only loss mechanism purposefully introduced is radiative recombination, which is unavoidable even in ideal conditions [27, Sec. 3.6.3]. The bandgap grading is introduced by means of a variation of the absorber composition along its thickness. To make the simulation realistic, this absorber composition profile must reflect the characteristics of the experimental setup used in this work. However, no prior knowledge about this relationship was available, so a guess had to be made. A gaussian profile was chosen as an *ansatz*, based on the fact that the annealing step used in this work to introduce this profile works analogously to diffusion doping from a finite solid source, where a gaussian doping profile is a solution to Fick's laws of diffusion [50, Ch. 7]. To account for the fact that the reactive $\mathrm{H_2S}$ gas is used during the annealing – which would be expected to induce some degree of resubstitution of Se for S or growth of purer-CZTS near the surface – a gaussian curve shifted towards the interior was also tested. Two sets of gradings were included: a total grading (i.e., $0 \leq x \leq 1$) and a partial, more moderate grading where $0.8 \leq x \leq 1$, as effectively achieved in the standard conditions of this work. The adequateness of these composition grading models was later tested using radiofrequency pulsed glow discharge time-of-flight mass spectrometry (rf-PGD-TOFMS). The resulting grading profiles are shown in Fig. 3.5 (a), and Fig. 3.5 (b) shows the effects of this grading on the band diagram of the cell. This diagram is similar to the one in Fig. 3.1 (b), except that here the contacts were assumed to be ohmic (the bands are flat). The impact of the bandgap grading on the IV curve of this ideal CZTSSe cell is shown in Fig. 3.5 (c). The results show that bandgap grading gathers the advantages of the two opposing cases – the high J_{sc} of a lower bandgap absorber (compare with the SQ limit curve for CZTSe) and the high V_{oc} of a higher bandgap absorber (as shown in the SQ limit curve for CZTS). A reduction in V_{oc} is seen in all grading examples since the increase in photogenerated carrier density is partially counter-balanced by an increase in the radiative recombination rate. The efficiency gains are higher for the case of total grading, as the corresponding bandgap variations achieved are larger[6].

Despite the demonstrated improvement in efficiency achieved by bandgap grading in the case of an ideal cell, the case is far more complicated in a real solar cell. For instance, a change in composition and in the position of the bands would alter the dynamics of recombination in defects. In

[6] It is possible that the efficiencies presented in Fig. 3.5 (c) are overestimated. This is due to the fact that SCAPS does not calculate the radiative recombination coefficient using internally consistent methods, but takes a user input value instead, which in this case was just an estimation. A more detailed model which consistently calculates this coefficient would produce more accurate results.

addition, an increase in the density of generated carriers would also increase instances of Shockley-Read-Hall and Auger recombinations. One could then predict that the efficiency improvements would not be as large as in the case of an ideal cell, and even efficiency reductions could in principle occur. To study this case, a real Mo/CZTSSe/CdS/ZnO/ITO cell was implemented. In the absorber layer, the following features were introduced: (i) radiative and Auger recombinations effects were allowed; (ii) Urbach tails in the conduction and valence bands, extending up to 0.2 eV into the gap, as reported in [9]; (iii) the single donor Zn_{Cu} and multiple acceptor V_{Zn} defects, which are characteristic of Cu-poor and Zn-rich growth conditions, were introduced with single energy levels as shown in Fig. 3.4 (b), which are also very similar in the case of CZTSe; (iv) a gaussian-shaped defect, positioned 0.8 eV above the valence band, whose origin is still unknown, but was observed in several state-of-the-art devices [9]; In the CdS layer, a double acceptor defect was included, modeling V_{Cd}, one of its most common deep defect, according to [51]. On the CZTSSe/CdS

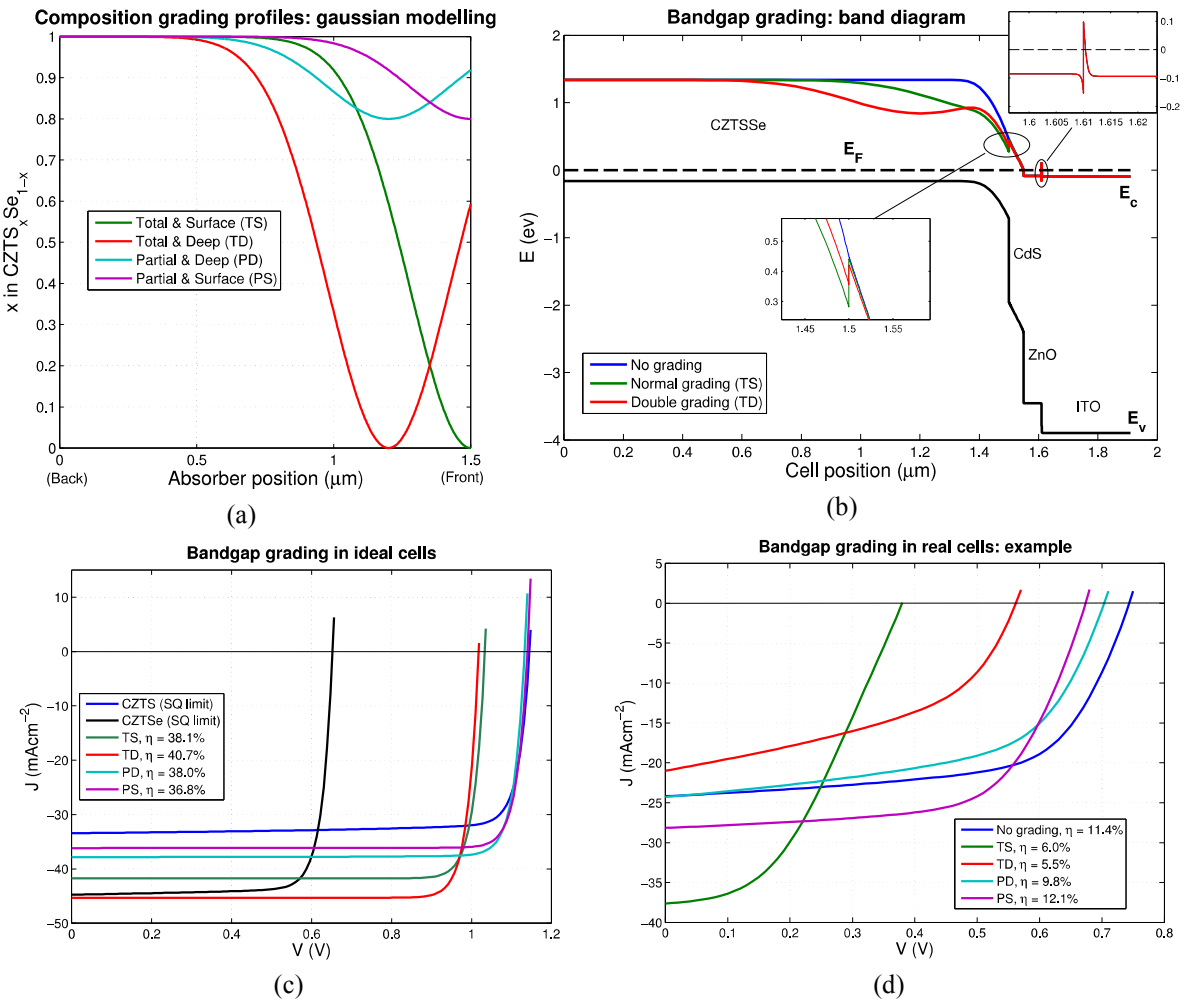

Fig. 3.5 – (a) Composition grading profiles tested as *ansatz*; (b) Band diagram showing the effect of composition grading on the conduction band. The insets show the conduction band offsets in the CZTS/CdS and ZnO/ITO interfaces; (c) Light IV curve for an ideal graded CZTSSe device and comparison with the Shockley-Queisser (SQ) limits for CZTS and CZTSe; (d) Light IV curve for a defect-saturated, real CZTSSe device. The SQ limit corresponds to pure-CZTS.

interface, a single defect center was positioned 0.2 eV above the valence band, close to what was tried in [52]. In ZnO, a double acceptor defect was incorporated, corresponding to the most common single defect V_{Zn}, as reported in [23]. The ohmic nature of the Mo BC and ITO FC was maintained. The results of the IV curve for different gradings are shown in Fig. 3.5 (d). The behavior is now completely different from the ideal case. All the gradings were actually detrimental for the performance of the cell, except the one corresponding to a partial grading starting from the surface (PS), where a slight increase in efficiency occurred. Some researchers also have alerted to the possibility of grading causing negative effects on the performance of a solar cell [53].

The results of this simulation illustrate that the effects of bandgap grading have more complexity than meets the eye. Boosting the efficiency of devices is possible, but the bandgap grading should be engineered according to very specific circumstances, not only general principles. Suggesting a favorable grading recipe upfront is certainly not trivial.

3.3. The CZTS/CdS interface and alternative buffers

The use of CdS and its interface with CZTS compounds is currently one of the hottest topics in the field, and is sparking debate among researchers. This is in part because it is believed to be connected to one of the major shortcomings of CZTS-based solar cells – their large V_{oc} deficit. While they already achieve a J_{sc} that is over 80% of the SQ limit, their V_{oc} deficit, defined by $V_{oc}^{deficit} = E_g/q - V_{oc}$, is still higher than in record CIGS devices, where $V_{oc}^{deficit} \leq 0.5$ eV, compared to $V_{oc}^{deficit} \geq 0.6$ eV in all CZTS compounds, with the case being worse for purer-CZTS devices [54]. This is the major issue limiting the efficiency of all CZTS-based solar cells.

Out of the several loss mechanisms in solar cells, shown in Fig. 3.6 (a), the two main factors

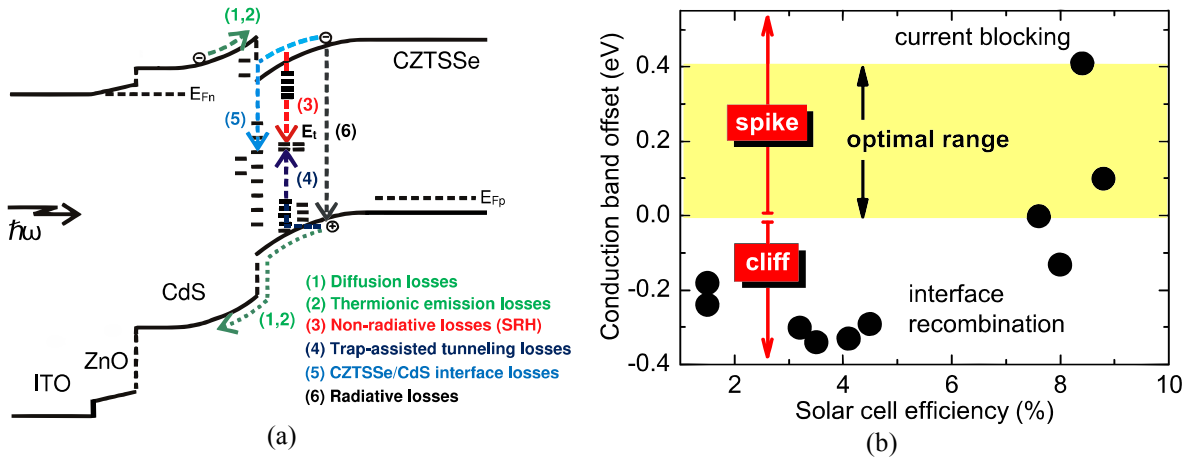

Fig. 3.6 – (a) Typical band diagram of CZTS-based solar cells with the most common loss mechanisms depicted. Adapted from [55]; (b) Conduction band offset measurements in state-of-the-art pure-CZTS cells. Reproduced from [52, Sec. Supplementary Material].

contributing to this $V_{oc}^{deficit}$ are bulk recombination and interface losses [56]. The occurrence of recombination in the absorber bulk was linked to a high density of defects, as was evidenced for example through photoluminescence studies [54]. Here, researchers explained the better performance of CZTSe compared to CZTS based on the lower populations and weaker effects of detrimental intrinsic defects [44], and on the less favorable physical properties of CZTS, such as a lower dielectric constant and larger electron effective mass, resulting in poorer carrier transport compared to CZTSe [19]. In the case of interface losses, the problem was, at first, thought to be associated with an unfavorable conduction band offset between CZTS and CdS, where the CdS conduction band would be lower than that of CZTS at the interface – a cliff-like alignment – which increases the probability of recombination at the interface and reduces V_{oc}. The opposite case – a spike-like alignment – is more favorable as it forms a potential barrier against back diffusion and thermionic emission of electrons from CdS. This barrier cannot, however, be too high, or it will impede the transport of the electrons generated in the absorber through the interface. A spike up to 0.4 eV is considered acceptable [19]. Yet, explaining the $\mathrm{V_{oc}^{deficit}}$ solely based on this is not satisfactory, as experimental measurements of this offset for devices with over 7% efficiency mostly yield either a spike-like or no conduction band offset [52], as is illustrated in Fig. 3.6 (b).

Therefore, the real reason behind this $V_{oc}^{deficit}$ is still an open question. Based on the frequent observation of bulk defects, it was mentioned that bandgap and electrostatic potential fluctuations could cause limitations in V_{oc} [54]. Some researchers speculated about the possibility of the Fermi level being pinned at the CZTS/CdS due a high density of interface defects, which could increase with the sulfur content in CZTSSe [9]. Others used ab-initio theoretical studies to suggest that intrinsic surface states exist in CZTS, which are not present in CZTSe, and that are not properly passivated by CdS, giving rise to interface states, explaining the dominating interface losses in CZTS compared to the dominating bulk recombination typical of CZTSe [52]. These two last trends indicated that an alternative buffer layer was a possible experimental improvement in the overall performance of devices, especially in the case of pure-CZTS. This has effectively been tried in the meantime, and it is interesting to see that record values of V_{oc}, with a $V_{oc}^{deficit}$ already on par with that of CIGS, were achieved with more than one type of alternative buffer material, namely $\mathrm{Zn_{1-x}Sn_xO_y}$ [57] and a hybrid $\mathrm{In_2S_3/CdS}$ [58]. Naturally, avoiding the use of the heavy metal Cd in favor of more environmentally benign elements would be preferable. For more on the merits of alternative buffer layers, see the discussion in [52].

In this discussion, the importance of the $\mathrm{Mo/CZTS}$ interface on the loss mechanisms is often not given the necessary attention, and sometimes even overlooked, as described in section 3.1. Nevertheless, the latest results are promising in the sense that they hint that CZTS-based solar cells could have a margin for further progression.

4. Experimental section

4.1. Mo back contact deposition

In the first step, the Molybdenum electrode is deposited on a 2 mm-thick, 3×3 cm^2 soda-lime glass (SLG) substrate using a magnetron-assisted DC sputtering machine. The process starts by a thorough cleaning of the substrates, through a rough mechanical cleaning, followed by a 2 minute bath in different solutions, with the sequence acetone-alcohol-deionized water, first in still solutions, and finally in an ultrassonic cleaner. The substrates are then dried using a compressed air flow, and stored in a muffle furnace at 50 ºC to remove any possible moisture remaining.

After the cleaning process, the substrates are loaded into the DC sputtering chamber, with a configuration as shown in Fig. 4.1. The chamber is evacuated into a base pressure of around 6×10^{-6} mbar. Before beginning the deposition of Mo onto the substrates, these undergo a further surface cleaning procedure of thermal degasification (desorption). This is achieved using a conventional 80 W tungsten halogen lamp to heat the substrates. Desorption is a thermally activated process and follows an Arrhenius-like dynamics, with a rate r_{des} given by [59]:

$$r_{des} = f \exp\left(-\frac{E_{des}}{k_B T}\right) \tag{11}$$

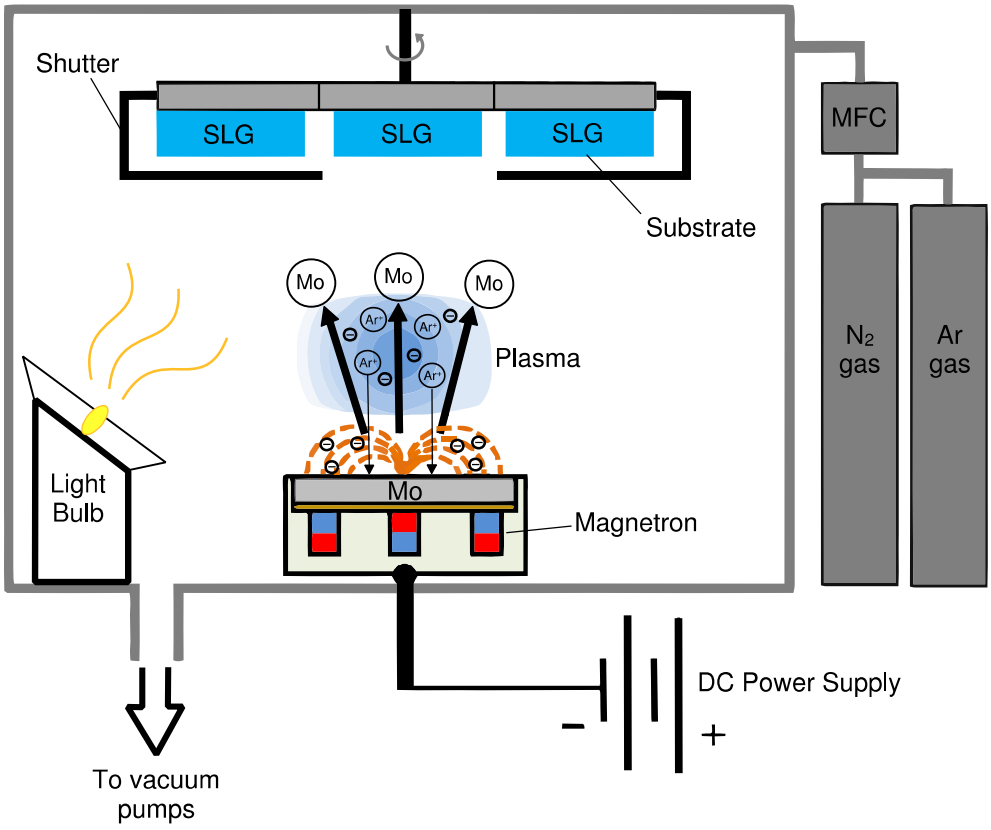

Fig. 4.1 – Schematic of the DC-sputtering machine for Molybdenum deposition (MFC – Mass flow controller).

where f is a function dependent on specific surface properties and desorption dynamics, E_{des} is the activation energy necessary for desorption, k_B is the Boltzmann constant and T the absolute temperature. The lamp used was capable of increasing the temperature to around 150 ℃, as measured by a thermocouple placed on the substrate holder plate. The deposition was started as soon as the pressure dropped back to close to the base pressure, to take advantage of the fact that the substrates retain a high temperature after the degasification process. Although no direct control of the temperature was employed, it was observed that it was close to 80 ℃ during deposition. This procedure was adopted since it leads to improved electrical properties and a greater Na content in the Mo films compared to depositions at room temperature [60]. The deposition was carried out during 1 min 35 s at a pressure of 6×10^{-3} mbar using Ar as working gas, with a flow of 30 mL/min. A power of 0.29 kW was set at the DC power supply. The substrate-target distance was fixed at 5 cm.

After deposition, the sheet resistance and adhesion of the Mo films were analyzed, through a four point probe system and a scotch tape test, respectively. A maximum sheet resistance of 1 Ω/□ was used as selection criterion. On the scotch tape tests, most films exhibited good adhesion. The thickness of the films was estimated at around 0.4 μm using a contact profilometer. When the films were stored for several days, they were cleaned by etching in deionized water prior to being used in the next step, to remove any molybdenum oxides formed on the surface.

4.2. Absorber layer production

The absorber layer fabrication in this work consisted of a two step process. First, a stack of precursors is deposited on the Mo-coated SLG, and then the precursor stack is annealed in the presence of a reactive gas to form the absorber.

4.2.1. Precursor stack

The precursor stack is deposited using a magnetron-assisted RF sputtering machine, as illustrated in Fig. 4.2. The system consists of a two-stage vacuum configuration assisted by a liquid N_2 trap. The chamber is evacuated into a base pressure typically between 3-5 $\times 10^{-6}$ mbar. Deposition was achieved by sputtering targets of ZnS, Cu and SnS_2, with 3 inches in diameter, and evaporating Se shots from a resistive heating evaporator. A constant flow of the working gas Ar was provided through a needle valve. The targets were sputtered simultaneously, with the substrate holder rotating counterclockwise and stopping above each target for a programmable amount of time. Two samples were prepared at each deposition, labeled *In* or *Out* according to their position on the sample holder. This configuration is illustrated in Fig. 4.3 (a).

The standard deposition layout consisted in a stack of precursors with the sequence ZnS/SnS_2/Cu repeated 8 times (a total of 8 periods), finishing with a layer of SnS_2 approximately 3

times the thickness of the corresponding interior SnS_2 layers (this configuration was based on previous work [61]), using a working power of $60/30/40$ W, respectively. Then, two different approaches for the inclusion of Se were chosen, as shown in Fig. 4.3 (b) and (c). In one of them, Se was included in the middle of every precursor period, with the sequence $ZnS/SnS_2/Se/Cu$. The resulting precursor type is hereafter labeled Se^{mid} precursor. In the other approach, Se was deposited as the uppermost layer, on top of the standard precursor periods, resulting in precursors henceforth referred to as Se^{top} precursors. The standard pressure used in the deposition was 4×10^{-3} mbar, and the chosen evaporation temperature for Se was 220 ℃, which is very close to the temperature at which its vapor pressure matches the deposition pressure used, according to data compiled by R.E. Honig (presented for example in reference [62]). The conditions described were the most frequent conditions used to fabricate precursors throughout this work, and shall be referred to as the standard conditions. Several of these conditions were eventually changed to test experimental hypotheses, and such changes will be explicitly mentioned for every case in the coming sections. The resulting precursors were characterized using scanning electron microscopy (SEM) in order to investigate their morphology. Their composition ratios were estimated using energy-dispersive spectroscopy (EDS), and Raman spectroscopy (with a 532 nm laser) was used in order to assess the phase evolution in the production process. Some thickness estimates were made using a contact profilometer, to evaluate thickness changes according to the type of precursor. The results of these characterizations and their analysis are presented in section 5.

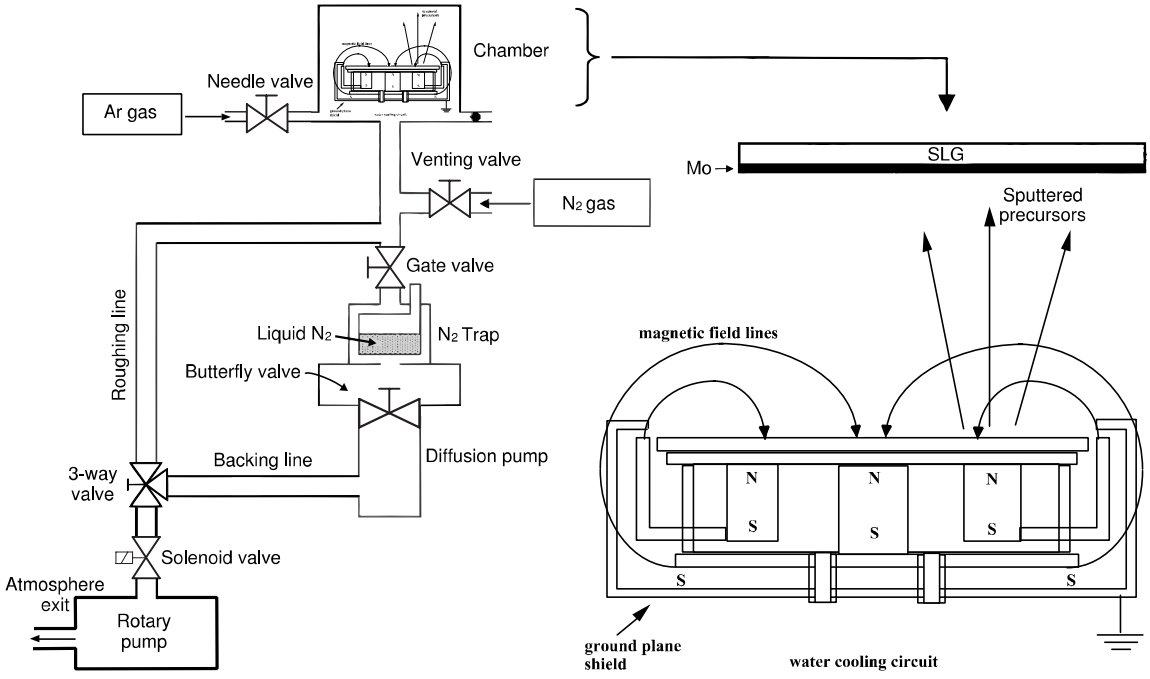

Fig. 4.2 – Illustration of the magnetron-assisted RF sputtering setup used to deposit the precursor stack. All vacuum valves are manually operated, except the solenoid valve.

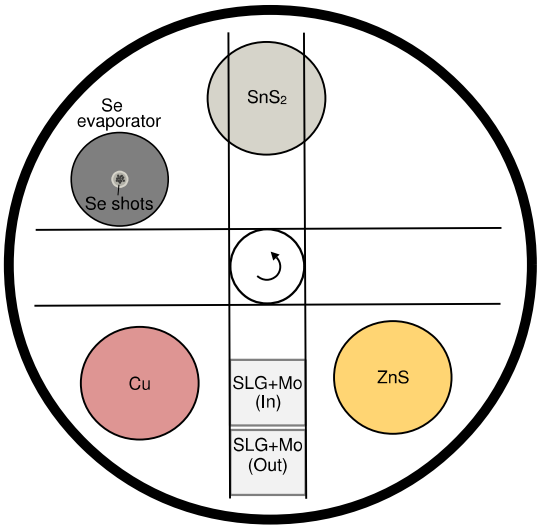

(a)

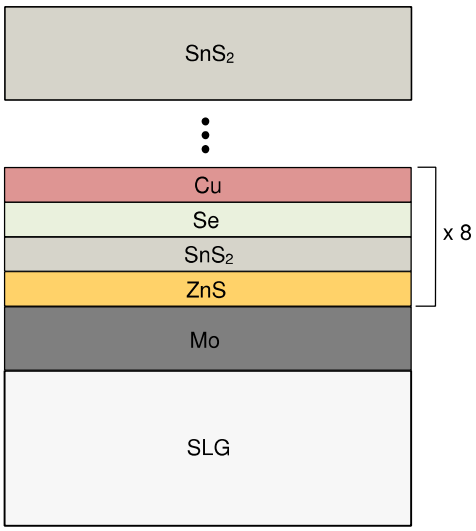

$\mathbf{Se^{mid}}$

(b)

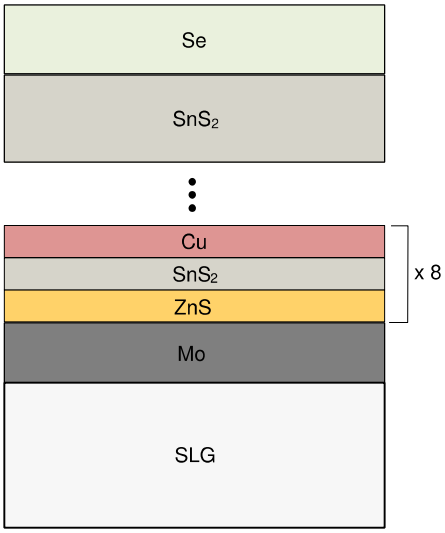

$\mathbf{Se^{top}}$

(c)

Fig. 4.3 – (a) The disposition of the sputtering targets inside the chamber of Fig. 4.2. The sputtering targets have 3 inches of diameter. The Mo-coated SLG substrates rotate counterclockwise to achieve the desired stacking sequence; (b) The Se^{mid} type of precursors, where Se is introduced in every precursor period; (c) The Se^{top} type of precursors, where Se is deposited only after 8 periods of the precursor stack, on top of them. Note that the layer thickness proportions in (b) and (c) are not necessarily accurate, and serve only as illustration.

4.2.2. Sulfurization of the precursor stack

The precursors described in the previous section are then loaded into an AnnealSys AS-One 100 rapid thermal processing/annealing (RTP/A) furnace, with a configuration as illustrated in Fig. 4.4. It consists of a chamber with steel walls cooled by water circulation, where the samples are placed on a graphite susceptor standing on quartz pins to thermally decouple it from the chamber walls. The temperature is measured using a thermocouple placed in contact with the graphite susceptor. The samples are heated using high power tungsten halogen lamps, with a programmable heating profile. The heating profiles attempted in this work were near trapezoidal, defined by an initial heating rate R_+, up to a plateau with a temperature T_P, maintained for a time Δt_P. The sam-

ples were then cooled down, which could either be forced cooling with a rate R_{-}, or natural cooling. The profile and corresponding notation are illustrated in Fig. 4.5. Forced cooling was achieved by supplying a certain amount of heat during the cooling process, and thus natural cooling was the fastest cooling achievable. The samples were processed at atmospheric pressure using a mix of $95\ \%\ N_2 + 5\ \%\ H_2S$ and N_2 as purging gas. H_2S is a toxic, corrosive and flammable gas (lower flammable limit of 4.3 %) [63], so an adequate exhaust system was coupled to the furnace to ensure a safe operation.

The resulting absorbers were studied in the SEM to analyze their morphology (grain size, compacity). EDS was used in order to determine the composition ratios and their evolution com-

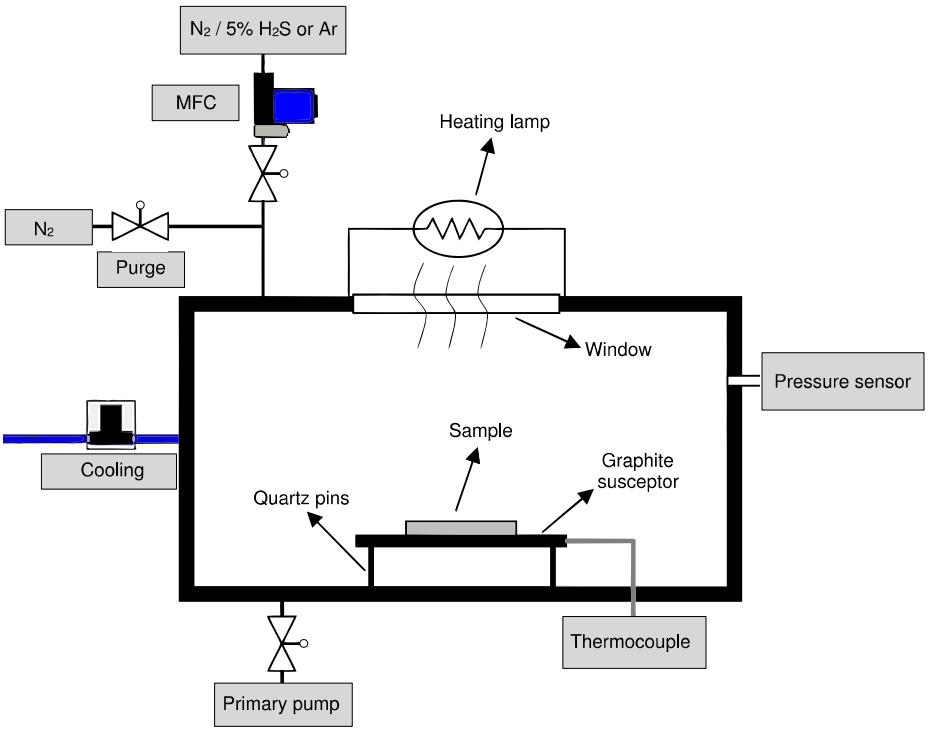

Fig. 4.4 – Sketch of the RTP/A furnace used in the precursor sulfurization step. All valves are electronically actuated.

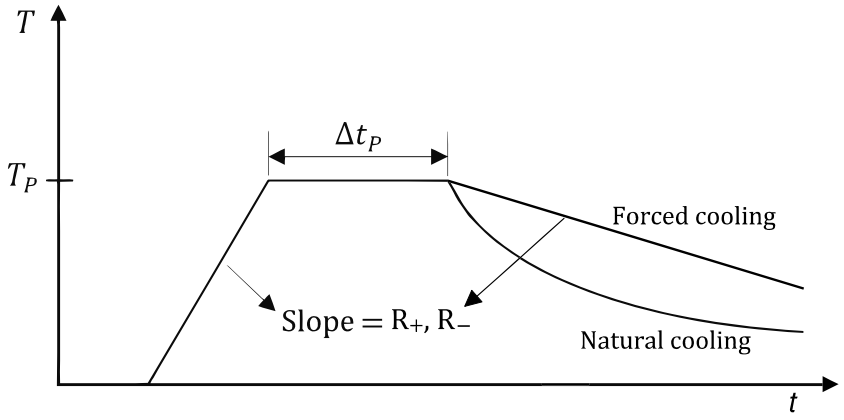

Fig. 4.5 – The thermal profile used throughout this work and the corresponding notation used.

pared to the precursors. The element distribution along the thickness of the absorbers was analyzed using rf-PGD-TOFMS. Finally, Raman spectroscopy was employed to qualitatively investigate the phase purity of the absorber and the presence of secondary phases.

4.2.3. Absorber etching in KCN

A chemical etching using Potassium Cyanide (KCN) was used in several samples produced in this work to remove any $Cu_x(S,Se)_y$ secondary phases present in the absorbers' surface, as recommended by literature [9]. The samples were immersed in an aqueous solution with a concentration of 5 wt.% (around 0.77 $mmolcm^{-3}$) of KCN for 2 min. Then, they were immersed in a solution of 50 % v/v of ethanol and deionized water for 2 min, to stop the reaction. Finally, they were put in deionized water for 2 min and then dried using an N_2 gas flow.

4.3. CdS buffer layer deposition

The buffer layer was fabricated using chemical bath deposition (CBD). In this work, Cadmium Acetate ($Cd(CH_3COO)_2$) was used as Cd source, Thiourea (CH_4N_2S) was used as S source and Ammonia Hydroxide (NH_4OH) was used as complexing agent. Different sources and complexing agents can be used, leading to different properties of the final CdS film (see for example [64]).

Aqueous solutions of 0.030 $mmolcm^{-3}$ of Cadmium Acetate, with a volume of 15 mL, and 0.60 $mmolcm^{-3}$ of Thiourea, with a volume of 10 mL, were prepared. Ammonia Hydroxide was

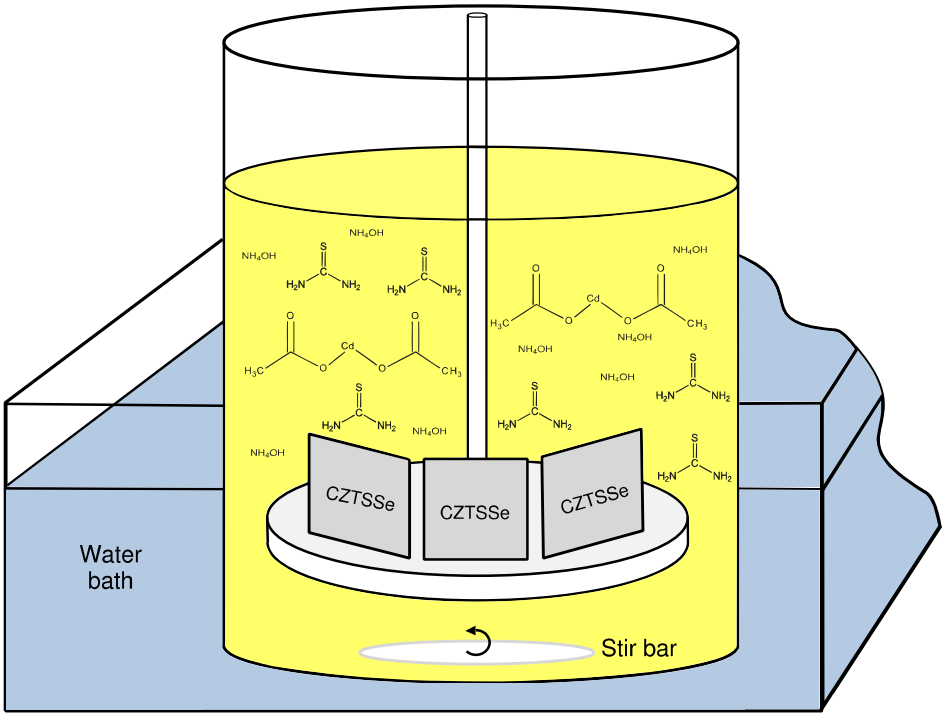

Fig. 4.6 – Illustration of the chemical bath deposition method used to deposit the CdS buffer layer.

used with a volume of 25 mL. The three reactants were mixed in the sample container in a quick sequence – first the Cadmium acetate, then the Thiourea, and finally the Ammonia Hydroxide. Then, the sample container was placed inside a water bath at 70 ℃, as shown in Fig. 4.6. Deposition was done for 12 min. After deposition, the samples were rinsed in deionized water and dried using a flow of N_2. The conditions mentioned should result in a thickness of around 50 nm, according to previous work.

4.4. ZnO and ITO window layers deposition

The window layers were produced using a PVD 75 Kurt Lesker magnetron-assisted RF sputtering machine, using i-ZnO and ITO targets with a diameter of 2 inches. The system is evacuated into a base pressure of around 4×10^{-7} Torr. First, ZnO is sputtered using a working power of 100 W and a pressure of 2×10^{-2} torr, using a mixture of above 97 % Ar and less than 3 % O_2, with O_2 being used as it improves the optical properties of ZnO (based on previous work). Lastly, ITO is deposited with a working power of 120 W and a pressure of 3.5×10^{-3} torr using Ar gas. The conditions chosen should result in thicknesses of ZnO and ITO around 60 and 300 nm respectively, based on previous measurements.

From four point probe measurements, the sheet resistance of the ZnO films exceeded the limit of the multimeters used, which was 200 MΩ/□. Considering that its thickness is 60 nm, we can estimate a minimum value for its resistivity of $\rho_{ZnO} > 12$ Ωm. Thus, we have the guarantee that this layer is resistive. For ITO, sheet resistances were typically 30 Ω/□.

4.5. Post-fabrication processing

After completing the device fabrication, solar cells with areas between 0.20 and 0.25 cm^2 were defined by mechanical scribing, and their IV curves were measured using an AM1.5 solar simulator. In addition, all completed devices underwent a post-fabrication annealing, done by placing the samples in a hot plate with a constant N_2 flow. The annealing temperature was 300 ℃, kept for 15 min. This step was implemented as it has been empirically discovered that it leads to considerable improvements in device performance, both in CZTS and in CZTSe (see for instance [65]). The post- and pre-annealing results were then compared.

5. Results and discussion

The first tests conducted were aimed at analyzing the evolution of the incorporation of Se in the Se^{mid} precursors, from an evaporation temperature of 180 ℃ up to the standard temperature of 220 ℃. The amount of Se (in atomic %) introduced in the precursors was estimated using EDS and the mass of Se evaporated was measured for reference using a weighing scale. The results were

as shown in Table 5.1. In one of the tests conducted at the standard conditions, the evaporation source was turned off only at the end of the precursor deposition, instead of after the final Se layer. This resulted in precursors with a higher content of Se and a larger evaporated mass, shown by (b) in Table 5.1. This test provided information about lateral contamination of the Se source during the deposition. It is thus expected that a non-negligible amount of Se might be present outside its position in the precursor stack (refer to Fig. 4.3 (b)). In the standard conditions, a mass of around

Table 5.1 – Study of the incorporation of Se in the Se^{mid} precursors at different evaporation temperatures. The uncertainties represent the standard deviation (within all standard Se^{mid} precursors) or a relative error of 5% as recommended for EDS in single elements [66] – whichever was bigger. Measurements marked with $(*)$ were done only once, so the uncertainties are the maximum deviation (for [Se]) and difference in two values measured in a weighing scale with an error of $\pm$ 0.1 mg (for m_{Se}). The difference between the In and Out positions is shown for the standard conditions.

	180 ℃	215 ℃	220 ℃
[Se] in Se^{mid} prec. (at. %)	0.5 ± 0.5 $(*)$	1.1 ± 0.7 $(*)$	(a) 29 ± 2 (In) / 36 ± 3 (Out) (b) 55 ± 3 $(*)$
m_{Se} evaporated (mg)	2.0 ± 0.2 $(*)$	11.3 ± 0.2 $(*)$	(a) $(25 \pm 3) \times 10$ (b) 793.3 ± 0.2 (*)

0.25 g was evaporated. To analyze this value, a simple estimate is presented. Let's assume that the corresponding thickness of all the Se layers in the precursors combined is of the order of the precursor thickness, about 1 μm. Given that their lateral dimensions are similar to the substrate's ($3 \times 3\ cm^2$) and assuming an average Selenium density of $4\ g/cm^3$, for simplicity, this corresponds to a mass of Se of $10^{-4} \times 9 \times 4 \sim 4 \times 10^{-3}$ g effectively incorporated in the precursors, which corresponds to less than 2 % of the evaporated mass. To make matters worse, a further amount of Se is lost during the sulfurization step, as will be discussed later. This poor efficiency in material use could limit the scalability of this process. Nevertheless, the simplicity and convenience of this method make it useful for initial small-scale laboratory research.

The initial composition of the precursors, shown in Table 5.2, was already close to the ideal values of (9), thanks to previous work conducted at the laboratory. However, these would often exhibit some structural and composition inhomogeneities, with the appearance of structures resembling dendrites, as shown in Fig. 5.1. These could be an indication of anisotropic growth conditions, and were found to be copper-rich using EDS. Throughout all the different precursor configurations implemented, these inhomogeneities could never be completely eliminated or controlled. Nevertheless, their presence did not appear to critically affect the resulting absorbers.

These precursors were then sulfurized using different profiles. For a complete set of the sulfurization profiles implemented, the reader is referred to Fig. 5.11, which serves as guideline.

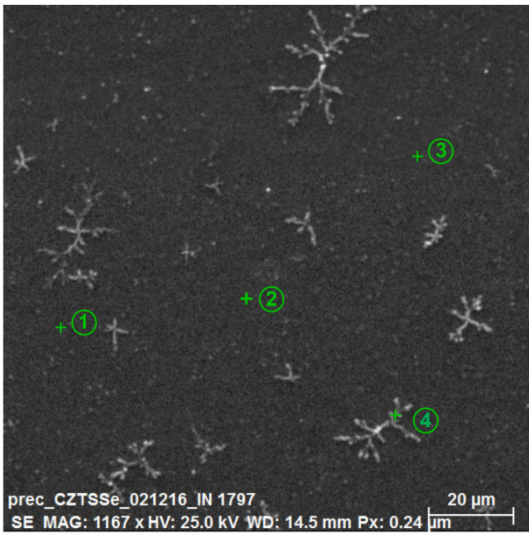

(a)

Table 5.2 – Spatial inhomogeneity of composition ratios in standard Se^{mid} precursors as measured by determination of atomic % of the respective elements through EDS.

	1	2	3	4
$\frac{\mathbf{Cu}}{\mathbf{Zn+Sn}}$	0.98	0.85	0.63	1.07
$\frac{\mathbf{Zn}}{\mathbf{Sn}}$	1.15	1.18	1.12	1.14

Fig. 5.1 – (a) Identification of the different regions analyzed by EDS. The dendritic-like regions appear to be copper-rich. (b) An image of the same precursor but corresponding to the Out position, showing the dendritic formations in greater detail. These appear to be present in depth and surface in certain regions. (c) A broader image corresponding to a third Se^{mid} precursor.

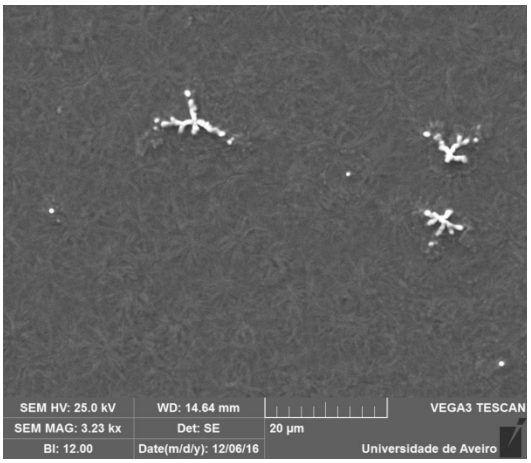

(b)

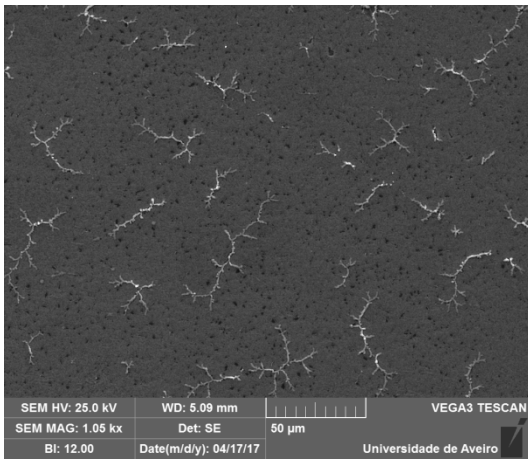

(c)

In the first sulfurizations, a constant profile was chosen, in order to observe the impact of the increasing amount of Se in the films. The samples were heated up to 200 ℃ with a first rate of $R_{+_1} = 0.5\ ℃/s$ and kept for 20 min. The idea behind this intermediate step was to promote some interdiffusion of elements between layers to improve the reaction kinetics in the next step, where a heating rate of $R_{+_2} = 0.5\ ℃/s$ up to 500 ℃ for $\Delta t_P = 10$ or 20 min was employed. Finally, forced cooling with $R_- = 0.5\ ℃$ until 300 ℃ followed by natural cooling was used. Right from the onset, the absorbers exhibited a very high concentration of surface blisters. At first, this was believed to be associated with the increasing amount of Se in the precursors – sulfurizations reached 500 ℃ and took place at atmospheric pressure, at which Se evaporates when temperatures reach around 670 ℃ [62], which indicates that some volatilization of Se could occur. However, the results ended up showing that the Se content alone cannot be responsible for the formation of these blisters, as will be evidenced throughout this section. Fig. 5.2 presents a comparison between the absorber morphology for different initial (precursor P) and final (absorber A) Se contents. The absorbers in

Fig. 5.2 (b) and (c) suffered the biggest loss in Se, and do not exhibit a higher blister formation or blister-induced damage. In addition, absorbers made from precursors with low Se content, shown in Fig. 5.2 (a), and even without any Se, shown in Fig. 5.2 (d), still exhibit blistering. Thus, the influence of Se in the absorber morphology was still not clear at this point.

Raman spectroscopy was used to investigate the resulting phases and their evolution with increasing Se content. Additionally, it was used to confirm the absence of peaks related to $Cu_x(S,Se)_y$ after the first set of absorbers produced was etched with KCN. The results are shown in

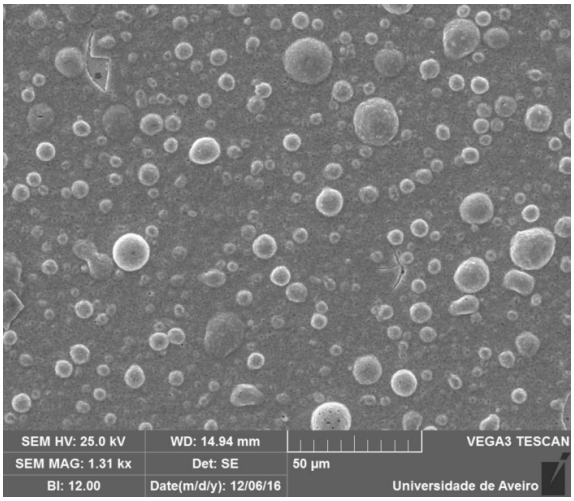

P: [Se] ~ 1 % → A: [Se] ~ 0.5 %

(a)

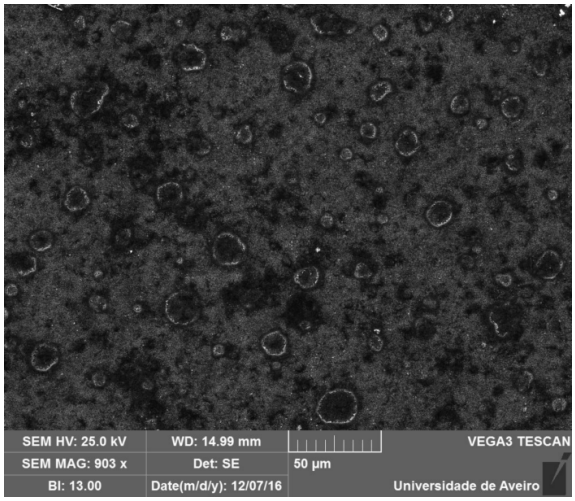

P: [Se] ~ 28 % → A: [Se] ~ 2.5 %

(b)

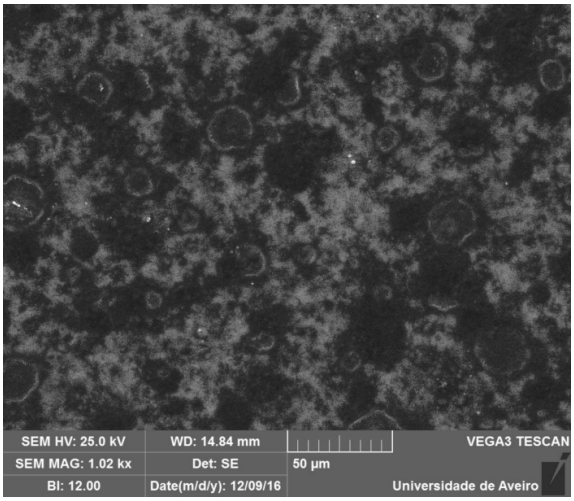

P: [Se] ~ 33 % → A: [Se] ~ 5 %

(c)

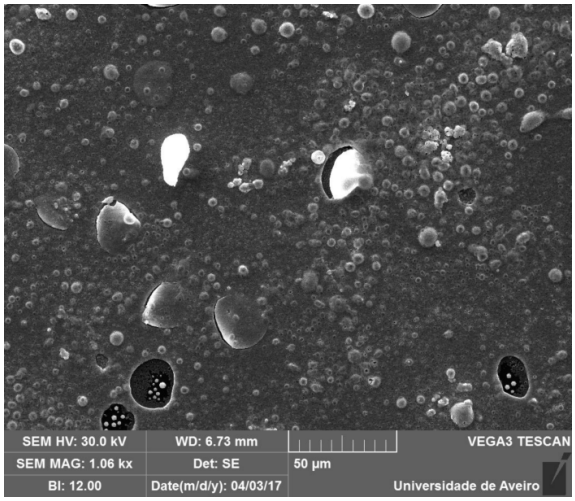

P: No Se (ideally) → A: pure-CZTS (ideally)

(d)

Fig. 5.2 – Comparison of different absorber morphologies with different contents of Se, highlighting that no apparent correlation exists between the increase in Se content and blister formation. Absorbers (a), (b) and (c) were produced with the same sulfurization profile, containing an intermediate step as described above, with $\Delta t_P = 20$ min in (a) and (b) and $\Delta t_P = 10$ min in (c). Absorber (d) ideally contains no Se, apart from possible chamber contaminations, and was sulfurized without the intermediate step, using only $R_+ = 0.5$ ℃$/s$, $T_P = 500$ ℃ , $\Delta t_P = 10$ min and natural cooling. It still exhibits blistering formation, proving that Se cannot be at least entirely responsible for this phenomenon.

Fig. 5.3. The results in Fig. 5.3 (a) show that the dendritic formations identified in Fig. 5.1 are likely to be a copper sulfide compound. A significant part of the absorbers produced did have $Cu_{2-x}S$ phases present, but no direct correlation between these occurrences and the dendritic formations could be observed. These phases were effectively removed using KCN etching, as Fig. 5.3 (b) illustrates. Due to its low Se content, the main peaks exhibited by the absorber correspond to CZTS.

It is also worth noticing that despite the uppermost layer of the Se^{mid} precursors being SnS_2, its characteristic peaks (the main one being around $314\ cm^{-1}$ [21, Ch. 4]) are apparently absent from the spectra of Fig. 5.3 (a). Considering the absorption coefficient of the absorbers, it can be estimated than the laser penetration depth should not be bigger than 200 nm. This could still be enough to probe and obtain signal from some precursor layers. However, given the number of precursor periods, each individual layer is very thin ($< 100\ nm$) and produces a weak Raman signal, which could be masked by background fluorescence. In order to study this in greater detail, a different excitation wavelength and power could be tried. Also noteworthy is the fact that Se-containing phases are present in the precursors, especially ZnSe, considering that elemental Se was used in the precursors and the Se layers were never in direct contact with the ZnS layers (remember Fig. 4.3 (b)). Similar results were found in other Se^{mid} precursors. Thus, within the reasonable doubt behind the assignment of the ZnSe phase to the peak near $254\ cm^{-1}$, this could also give some qualitative information about lateral Se contaminations during deposition.

The resulting absorbers were used to fabricate solar cells. The results for the two best devices fabricated are shown in Fig. 5.4 and Table 5.3. One of the most striking features of these results is

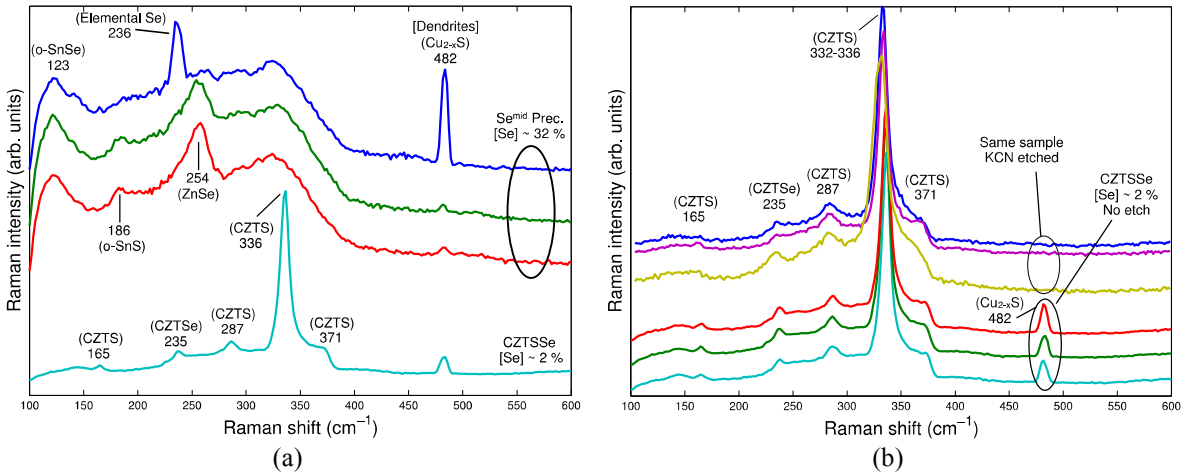

Fig. 5.3 – (a) Raman spectra of a typical Se^{mid} precursor. The upper spectrum (dark blue) was taken in the vicinity of a dendritic formation, and shows a strong peak associated with copper sulfide phases. The lower spectrum corresponds to a CZTSSe absorber with around 2 % Se resulting from standard Se^{mid} precursors, for comparison; (b) Different spectra of the same CZTSSe absorber shown in (a), taken in different regions as identified in optical and electron microscopy. The upper spectrum (dark blue), corresponds to a blister. It can be seen that the composition is uniform despite the morphological inhomogeneities. Another set of spectra in the same absorber after KCN etching, presented to confirm the removal of the unwanted $Cu_{2-x}S$ secondary phases. Peak identification was based on work compiled in [21, Ch. 4], [67].

the significant difference introduced by the post-fabrication annealing. Non-annealed devices showed rectifying behavior and photovoltaic effect, but exhibited very poor efficiencies in the latter (almost always below 0.2 %), while many of the corresponding annealed devices improved their photovoltaic parameters – as Table 5.3 shows, the champion devices improved all of them. However, these improvements could not be seen in some devices and, in some cases, the performance of some devices even deteriorated after the annealing, as will be shown later in this section. In general, the effects of post-fabrication annealing are still largely unknown. Essentially every different post-fabrication annealing possible has been tried recently – immediately after absorber production (before further processing), after the CdS deposition, and on complete devices, such as implemented in this work [65]. As of yet, no generally accepted explanation or improvement mechanism has been found. Several hypothesis have been suggested, namely changes in Na content (in the absorber and/or in the pn junction region), oxidation of grain boundaries, reduction in the concentration of the $[Cu_{Zn} + Zn_{Cu}]$ defect cluster and changes in the $S/(S + Se)$ ratio. For more on this topic, the reader can see for example [18], [65] and respective references. No further discussion on the post-fabrication annealing implemented in this work will be done, as it was an experimental step implemented on an *ad hoc* basis, and was not subject to a systematic study, which would be outside the scope of the present work. Any explanation presented would thus be no more than a conjecture.

Despite several other standard Se^{mid} precursors being produced, which were then sulfurized using the same profile, their corresponding device results were poor (with efficiencies below 0.4 %, regardless of post-fabrication annealing), indicating that some inhomogeneities could be affecting the reproducibility of the results. One such case is blister formation, which is an uncon-

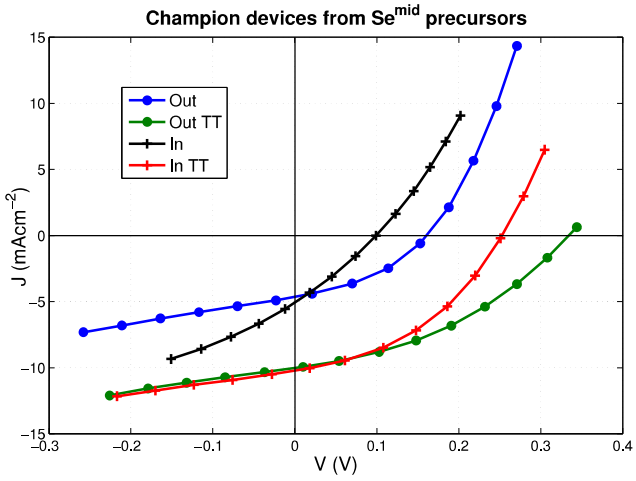

Table 5.3 – Device parameters for the champion devices resulting from Se^{mid} precursors, before and after post-fabrication thermal treatment (TT).

	V_{oc} (mV)	J_{sc} (mA/cm^2)	FF (%)	η (%)
Out	161	4.6	38	0.28
Out TT	334	10.0	39	1.30
In	99	5.1	28	0.14
In TT	252	10.2	41	1.07

Fig. 5.4 – Light IV curves for the champion devices fabricated from standard Se^{mid} precursors. The devices were based on the In and Out positions of the same precursor, containing [Se] ~ 30 % in the In and [Se] ~ 38 % in the Out. The absorbers were etched in KCN and had $S/(S + Se) \sim 0.93$ and 0.91 in the In and Out, respectively. Although the composition ratios varied slightly from precursor to absorber, their values were still near those described in Table 5.2. Post-fabrication annealing was done at 300 °C.

trollable process systematically occurring. The better results of the devices shown in Fig. 5.4 might be associated with a lower blister induced-damage, either through a lower blister concentration or by having blisters that only burst superficially and still preserve a certain film thickness underneath them. Fig. 5.5 shows some of the morphological aspects of these champion absorbers. Both in the In and in the Out positions a number of burst blisters can be found. EDS analysis in these blisters showed that no absorber film remains on their interior, and only the Mo from the BC is present, which becomes exposed and reacts with S during sulfurization to form MoS_2.

Once they burst, these blisters expose the BC of the device, which will then be in direct contact with the buffer and window layers. These contacts constitute shunts within the device, which

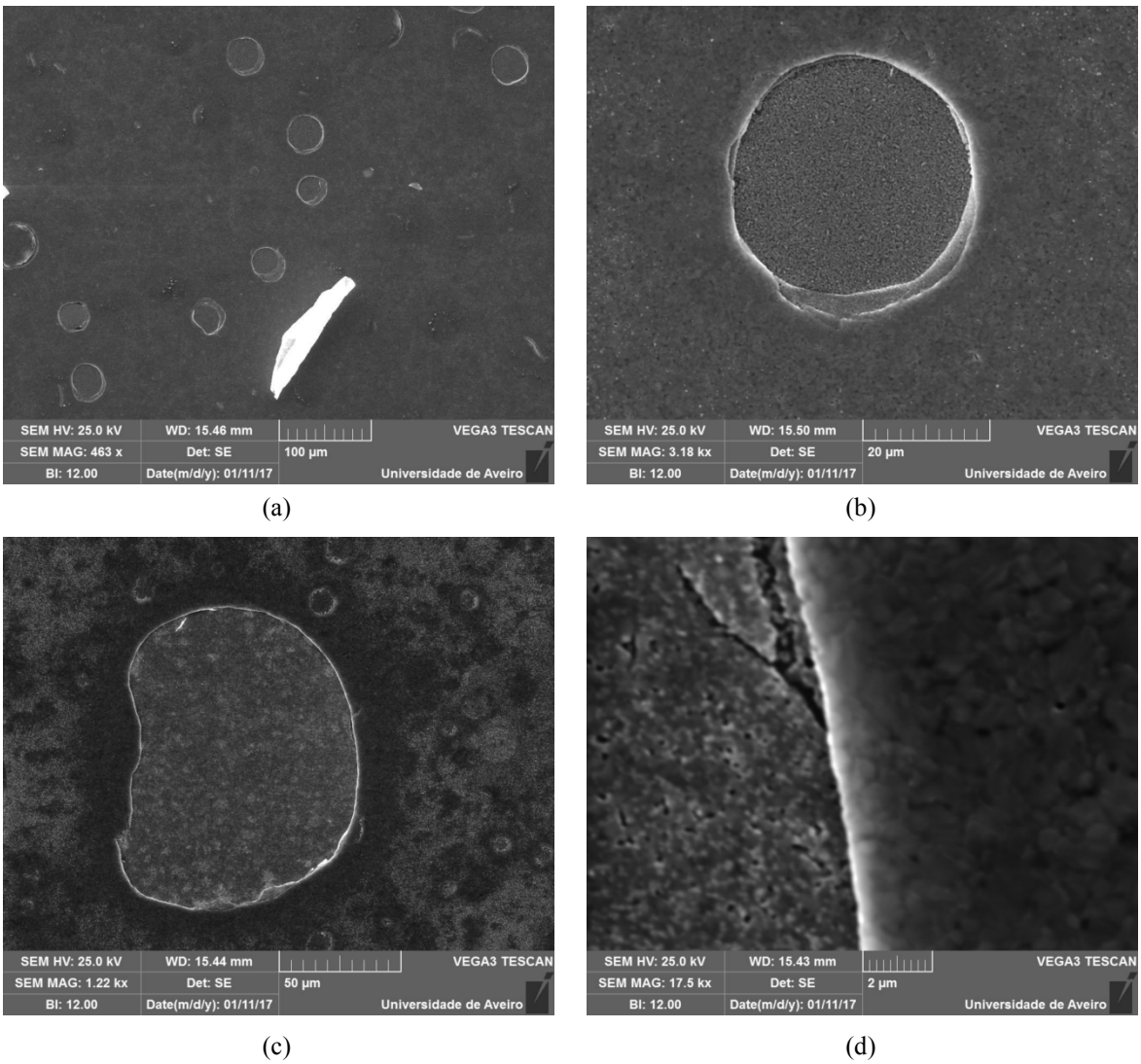

Fig. 5.5 – Details of the morphology of the champion absorbers of Fig. 5.4, prior to KCN etching. (a) and (b) were taken at the In position, while (c) and (d) correspond to the Out. On (b), notice the detail on the border of the blister, showing that several layers of the film were affected by it. EDS results on this blister show that it is mostly constituted by Mo and S, with no absorber film remaining. In (c), a burst blister similar to (b) can be seen, along with smaller ones, located nearer to the surface of the film. In (d), a magnified image of (c) is presented, showing details of the grain size of the absorber and of the interface with the blister.

can only be blocked by the resistive i-ZnO layer provided that their total area remains by orders of magnitude smaller than the absorber area. Otherwise, these shunts will become the dominant current pathway within the device, with a low characteristic shunt resistance R_{sh}, significantly deteriorating the photovoltaic efficiency. As Fig. 5.5 shows, despite having achieved efficiencies over 1 %, the best performing devices are still significantly affected by blistering. Thus, controlling blister formation in the experimental procedures used should be a fundamental step towards improving the quality of the devices, and became the main focus of this work. At the same time, finding a way to incorporate a higher amount of Se in the final absorbers is crucial for the purpose of bandgap grading, and this could not yet be achieved, as all absorbers had an Se content under 3 %. In order to do this, the loss of Se during sulfurization must be prevented.

Since both the blister formation and Se loss occur during sulfurization, changing its procedure should be the most obvious solution. In order to gain more insight on this, the following tests were devised. Precursors with a low Se content (evaporation temperatures of 180 and 215 ℃, see Table 5.1) were sulfurized using the profile described in the beginning of this section, but were removed after the intermediate step (heating to 200 ℃) and analyzed in the SEM. The precursor with lower Se content was then sulfurized again, now using the complete profile, along with an equal precursor which had not undergone any sulfurization yet (the original precursor was divided into smaller parts to achieve this), for comparison. The results, shown in Fig. 5.6, reveal a clear trend. After the intermediate heating step, the precursors exhibit defects that are not present initially, as shown in Fig. 5.6 (a) and (b). Their low contrast and definition also hints that they are found deep within the precursors. Fig. 5.6 (c) and (d) show, respectively, the absorbers corresponding to the precursor of Fig. 5.6 (a) and its corresponding untouched half, that underwent a full sulfurization profile simultaneously. By comparison, it can be deduced that the intermediate step aggravates the blistering formation and bursting. Notice that, in Fig. 5.6 (b), new blisters can by seen forming inside blisters that had burst, showing that the process was ongoing and far from equilibrium. Again, this behavior cannot be simply attributed to the amount or to the loss of Se. Even though an increase in the density of defects is seen in Fig. 5.6 (b) compared to (a), attributing it simply to the fact that the corresponding precursor is slightly richer in Se would then run into an apparent contradiction when considering the results of Fig. 5.2 (b) and (c) or Fig. 5.5, where the absorbers lost a much higher amount of Se and exhibit less blistering, or only superficial blistering. A more fundamental justification for this behavior had to be searched. Following the information gathered from this test, the intermediate sulfurization step and the forced cooling were abandoned, to try to reduce the impact of blistering and the loss of Se.

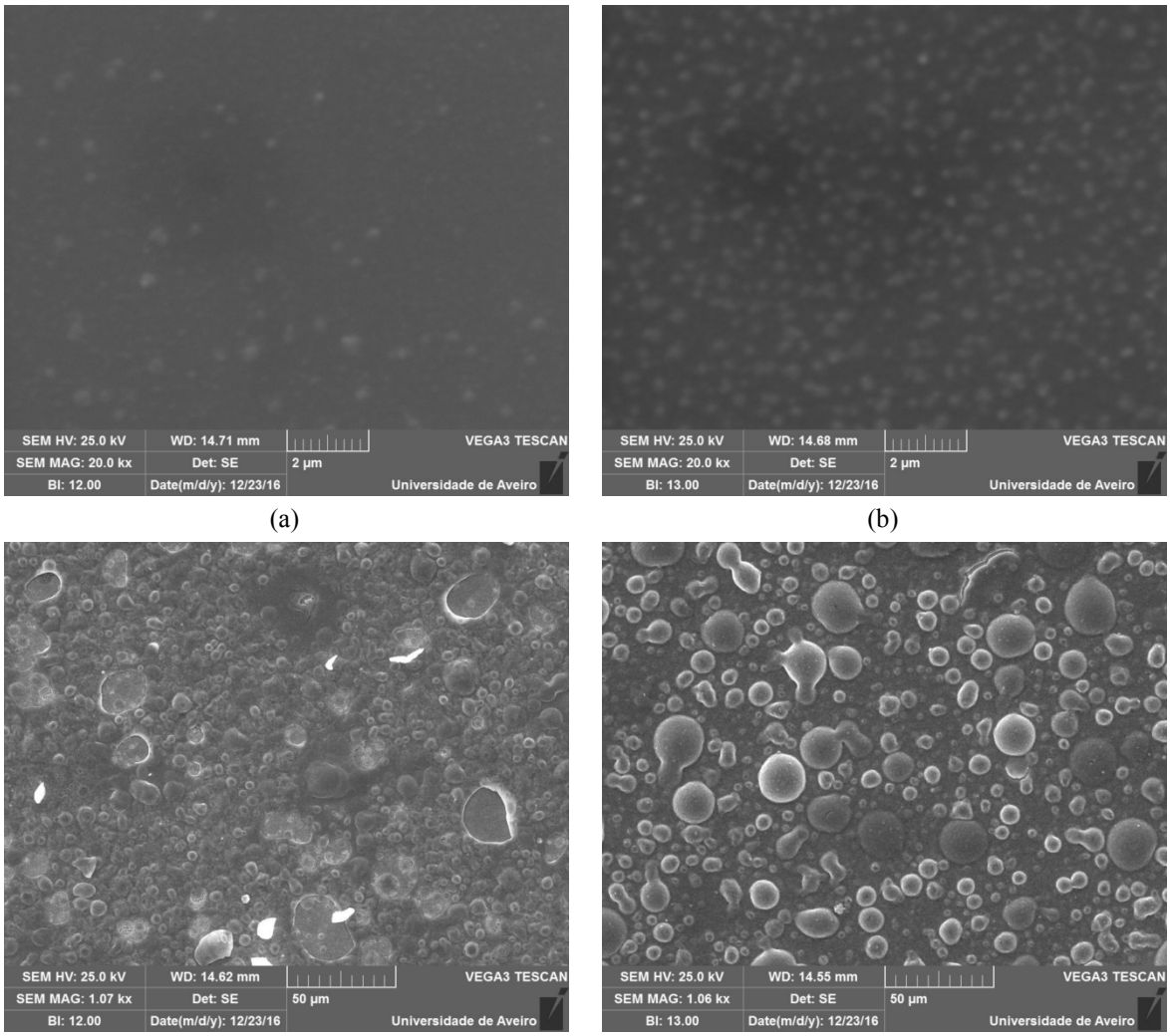

Fig. 5.6 – (a) and (b) show the morphology of two different precursors sulfurized using only the intermediate step of heating up to 200 ºC; (c) and (d) show, respectively, the resulting morphology of a complete sulfurization of the precursor in (a) and of a piece of the same precursor, but untouched.

Another test was tried, which was aimed at understanding whether the sulfurization chamber configuration had any influence on the problems exhibited by the absorbers. In principle, one could associate these problems with many intrinsically experimental aspects – for instance, inaccurate temperature readings, temperature inhomogeneities on the surface of the samples, or a thermal gradient caused due to the furnace lamps illuminating the surface of the precursors directly, while these are at least partially thermally decoupled from the graphite susceptor (where the temperature is measured), since the substrate of the precursors is a 2 mm-thick glass. Although somewhat farfetched, these possibilities were tested as part of a troubleshooting approach. A very simple change was made in the sulfurization configuration – the precursors were introduced upside down in the chamber, that is, with the surface of the precursor facing the graphite susceptor. This approach was later refined by placing the samples on a clean glass substrate instead of directly on the

graphite susceptor, to avoid contamination of the surface. The resulting absorbers were labeled Up or Down according to this sulfurization configuration (the Up mode being the standard one).

Incidentally, it was discovered that with this small change the final amount of Se in the absorbers could be significantly increased. In the Up absorbers, the maximum amount of Se reachable was always below 5 %, while in the Down absorbers this amount could be varied between 0 and over 16%, corresponding to an average variation in the $S/(S+Se)$ ratio from 1 to near 0.5. Raman analysis, shown in Fig. 5.7, confirmed the presence of the characteristic CZTSe peaks with intensity increasing with the Se content. Additionally, it can be seen that the dominant peaks (corresponding to the A_1 modes of CZTSe and CZTS, in Schoenflies notation), are shifted relative to the position of the respective pure compound. The explanation for this behavior was provided by Adachi [21, Ch. 4]. The A_1 modes of CZTSe and CZTS correspond to anion (Se-Se and S-S) vibrations, with the cations remaining motionless. Considering a classical description of a simple linear oscillator, the intersubstitution of S and Se change the mass of the oscillating system – higher masses (higher Se contents) shift the frequency of oscillation to lower values, and the opposite happens for higher S contents. This has been reported already [68], and three different groups of researchers [69]–[71] have proposed the use of this frequency shift as a way to determine the $S/(S+Se)$ ratio in CZTSSe. This would be a relatively easy and non-destructive method which could provide more accurate estimations compared to EDS. For instance, accurate measurements of this ratio using EDS are difficult because there is an overlap between Mo and S lines, and both S and Se can be present as $Mo(S,Se)_2$, as has already been discussed in section 3.1, which are, in this case, wrongly accounted for in EDS [45]. Since the spectra in Fig. 5.7 correspond to point measurements in dif-

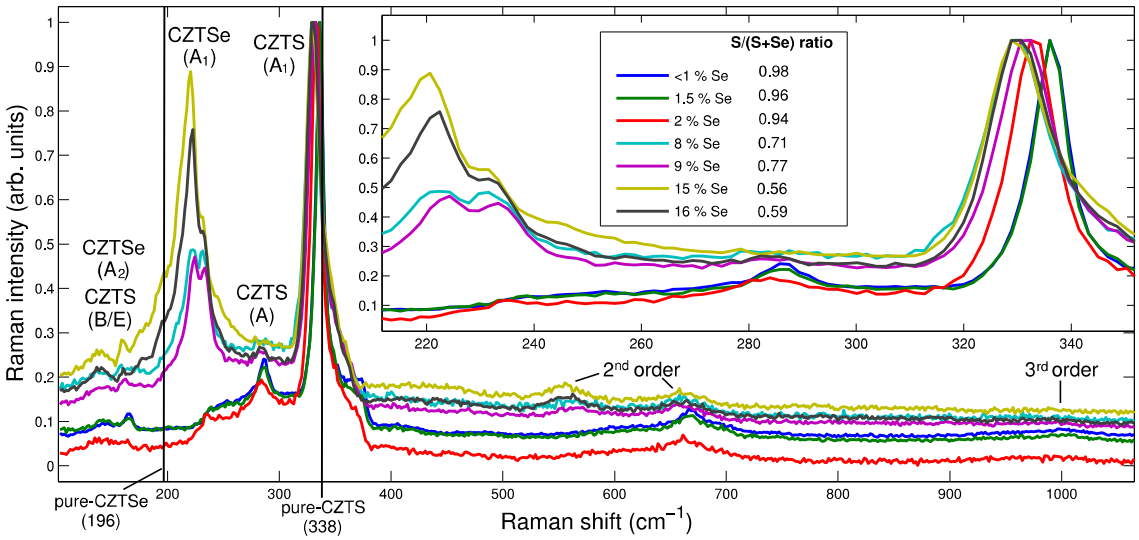

Fig. 5.7 – Raman spectra of some of the absorbers produced, with identification of the modes according to Schoenflies notation. For reference, notice the black vertical lines, which are the Raman peaks of the dominant A modes of pure CZTSe and CZTS – 196 and 338 cm^{-1}, respectively [21, Ch. 4]. The inset is a zoom-in on the region corresponding to the dominant A_1 modes. The Raman shifts clearly correlate with the S/(S+Se) ratio as estimated by EDS.

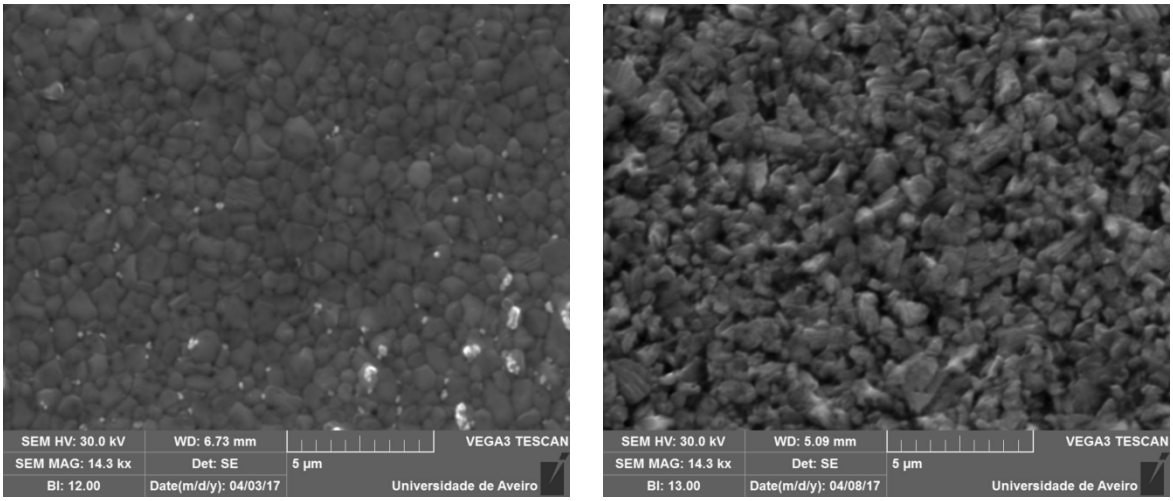

(a) (b)

Fig. 5.8 – SEM images of two different absorbers detailing their good crystallinity, given by a compact structure with micrometer-sized grains. (a) corresponds to pure-CZTS (ideally), while (b) corresponds to CZTSSe with around 9% Se.

ferent samples, the Raman shifts indicated have a significant uncertainty. By producing a higher number of samples and performing a statistical analysis on the Raman shift in different absorber locations, to account for possible lateral inhomogeneities in the Se or S content, a rigorous calibration could be provided for determining the $S/(S+Se)$ ratio, using the methods described in this work, between a content of Se between 0 and approximately 16% as measured by EDS, corresponding to a $S/(S+Se)$ ratio from 1 to as low as around 0.5. In Fig. 5.7 it can also be seen that it appears that the peak corresponding to the CZTSe A_1 mode is splitting with increasing amounts of S. Since there is no secondary phase in the CZTS or in the CZTSe system with a Raman mode in this region, this behavior is unknown. Notice that the same result was observed in [71], but no explanation was given.

Another noteworthy aspect in Fig. 5.7 is that the second order scattering of the main modes was also detected, and in some cases even the third order. These correspond to the simultaneous excitation of two and three phonons, respectively, and give a qualitative indication of good crystallinity. See for example Fig. 5.8, which shows SEM images of absorbers with high and low Se contents, detailing a compact film and grain size close to 1 µm.

Despite the improvements achieved with this method regarding the losses on Se in the absorbers, the problem of blister formation persisted, and still no clear trend could be observed through the comparative analysis of the morphology of the absorbers. The problem of blister formation is discussed in depth on subsection 5.1.

Blister formation dynamics was also studied by using Se^{top} precursors. Initially, this precursor configuration was envisioned as an alternative to Se^{mid} precursors to achieve a composition grading in the absorbers. However, given the systematic occurrence of blistering, this configuration was

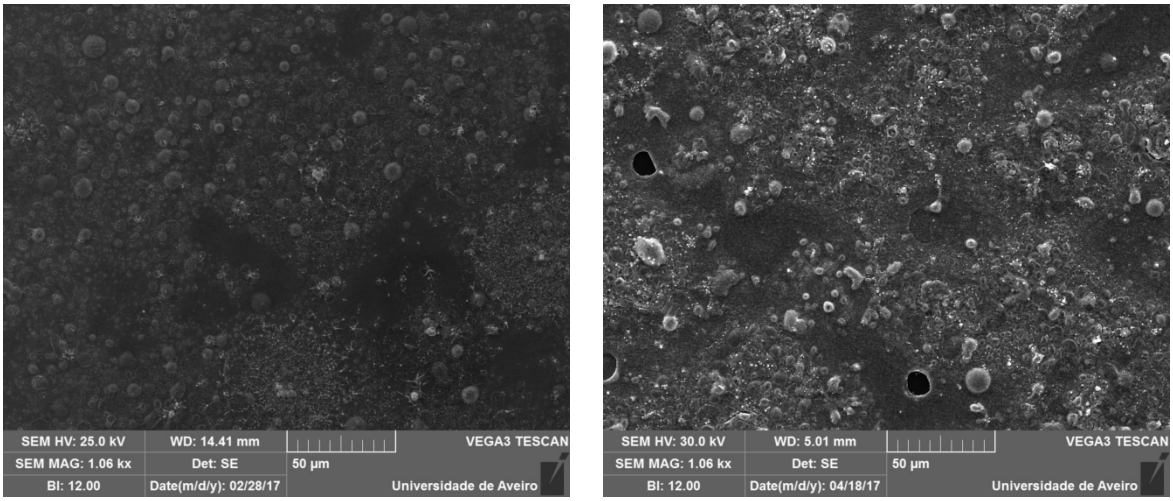

(a) (b)

Fig. 5.9 – SEM images of two different absorbers, non-etched, produced from different standard Se^{top} precursors. Absorber (a) was sulfurized using $R_+ = 5$ ℃/s, $T_P = 520$ ℃, $\Delta t_P = 20$ min and natural cooling, while (b) the conditions were $R_+ = 0.2$ ℃/s, $T_P = 500$ ℃, $\Delta t_P = 20$ min and natural cooling. In both cases blistering can be seen.

tested alongside the Se^{mid} configuration, replicating some of same conditions tried initially with Se^{mid} precursors, to try to gain further insight on blister formation mechanisms. The standard Se^{top} precursors had a content of Se of (17 ± 2) %, corresponding to an evaporated Se mass estimated as $(8 \pm 2) \times 10$ mg. The first tests conducted still revealed the occurrence of blisters, and again no trend could be understood from the results. Fig. 5.9 shows two different results for Se^{top} precursors sulfurized using different conditions, but exhibiting similar results in terms of blistering.

To summarize the information gathered up to this point, the results of the troubleshooting tests conducted showed that: (i) The loss of Se cannot be the sole responsible for blister formation, and might not be responsible for it at all; (ii) Blisters do not represent secondary phase segregation and still exhibit the kesterite structure in Raman, except when they burst throughout the whole thickness of the film, in which case the Mo BC becomes exposed and reacts with H_2S; (iii) Blister formation is aggravated when an intermediate heating step to 200 ℃ is used, meaning that the blister formation mechanism is active already during the heating process and not only at plateau temperatures; (iv) Blistering is not caused by inaccurate temperature readings or by the presence of a temperature gradient between the surface of the samples and the graphite susceptor; (v) Blistering is not hindered or reduced by changing from Se^{mid} to Se^{top} precursors. However, still no appropriate explanation for this phenomenon could be given. This topic is further discussed in the next section.

5.1. The problem of blister formation in CZTS

The reports of blistering occurrence and blister formation in CZTSSe in literature were analyzed in this work, and were found to be surprisingly scarce given the frequency of occurrence and impact of this problem. As far as could be investigated, there are only two comprehensive studies

dealing with blister formation, both in pure-CZTS, by Malerba *et al*. [72] and Bras *et al*. [73]. The occurrence of blister-like formations was mentioned in [9] and labeled as "bumps", but it was mentioned that these were only present when annealing was done in an inert atmosphere, and disappeared when H_2S was used during annealing, which is obviously not a satisfactory explanation in the present case. In another work, Katagiri *et al* mentioned that «The surface of the CZTS films (…) could be seen quite rough and there were many voids (…) », which was linked to the occurrence of Sn "hemispheroids" on the surface of the ZnS layers in a precursor sequence of SLG/ZnS/Sn/Cu, that disappeared when the sequence was changed to SLG/ZnS/Cu/Sn [74]. The authors did not provide any explanation or additional studies in this regard.

In the two complete studies dealing with blistering formation, different explanations were given. Bras *et al.* mentioned that this problem had been reported previously in the deposition of metallic films and also compounds such as GaN and $TaSi_2$ produced using sputtering or ion bombardment followed by high temperature annealing, and it was generally accepted in those cases that blisters were formed due to the entrapment of Argon gas within the films during deposition, which was then released at high temperatures, forming blisters through coalescence or Ostwald ripening, depending on the temperature and duration of the process (see [73] and respective references). It is known that this entrapment can occur during sputtering due to recoil implantation – a small fraction of the Ar ions which hit the cathode during sputtering can be backscattered all the way towards the deposited film and lodge in it, provided that they have a high enough energy. One way to minimize this problem is increasing the sputtering pressure, which reduces recoil implantation by increasing the scattering of Ar atoms in their path towards the film. This was implemented by Bras *et al.*, and a decrease in blistering was achieved. The presence of entrapped Ar in the films after sputtering was measured using EDS based on the $K\alpha_1$ and $K\alpha_2$ lines of Ar, which occur just slightly under 3 keV [75], and Ar signal was found to decrease with increasing sputtering pressure. Using this information, the EDS spectra obtained in the present work were analyzed, comparing precursors with corresponding absorbers in the region near 3 keV. However, the results were unclear. In all cases, any signals present in this region had very low intensities and signal-to-noise ratios, making it difficult to distinguish possible variations. Besides, there is an overlap between the mentioned Ar lines and the Ll line of Sn – these lines are separated by less than 90 eV [75], lower than the energy resolution of EDS, which although it depends on the detector used, is usually above 100 eV [66, Ch. 7]. Thus, this method has weak statistical grounds and could not be applied in the present work. In the other study, Malerba *et al*. found evidence that blistering was occurring due to a stress-driven viscoplastic deformation associated with the presence of compressive stress in the precursors, as measured by X-ray diffraction and surface curvature methods [72]. The occurrence of tensile or compressive stresses in film depositions by sputtering is known to be directly related to how ener-

getic the process is (see for example reference [76]). In qualitative terms, within the pressure ranges of plasma stability, when the pressure is low the sputtered atoms are subject to lower scattering events, and reach the substrate with higher energies, forming a more compact film, subject to compressive stress. By increasing the sputtering pressure used in the precursor deposition, Malerba *et al*. were also able to demonstrate a significant reduction in blister occurrence in pure CZTS.

Although basing their results on different hypothesis, Malerba *et al*. also mention that the two mechanisms are not mutually exclusive. Remarkably, both groups determined that in order to avoid blister formation in CZTS, a pressure value close to 10^{-2} mbar would be ideal. For pressures near 4×10^{-3} mbar, as used in the present work, both groups predict the occurrence of severe blistering. In light of these findings, it was decided to implement a series of tests using precursors deposited at higher pressures.

Some preliminary tests were conducted using the recommended sputtering pressure of 10^{-2} mbar. However, due to technical limitations of the experimental equipment used, the same precursor conditions in terms of thickness and composition could not be easy replicated, so an intermediate pressure of 6×10^{-3} mbar was used instead. According to the results of Malerba *et al*. [72], this change should be big enough to see a significant reduction in blister density in the films. The $\mathrm{Se}^{\mathrm{top}}$ configuration was chosen, and some adjustments were made in the sputtering conditions to recalibrate the precursors – total deposition time had to increase in order to maintain the same film thickness, since the higher scattering that occurs at higher sputtering pressures also leads to lower deposition rates. The individual layer times were adjusted proportionally to maintain the ideal composition ratios. The Se evaporation temperature was increased to 225 ℃ to compensate for the higher deposition pressure. The corresponding evaporated Se mass was 63.6 ± 0.2 mg, which is within the typical values of standard $\mathrm{Se}^{\mathrm{top}}$ precursors. The thickness of the resulting precursors was measured using a contact profilometer, and was found to be around 0.9 µm. In comparison, the thickness of a standard $\mathrm{Se}^{\mathrm{mid}}$ precursor, which has a larger amount of Se, was measured to be around 1.4 µm. Thus, this thickness was considered acceptable for comparing results.

The results of the tests using precursors deposited at the pressure of 6×10^{-3} mbar are shown in Fig. 5.10. The results strongly suggest that the change in sputtering pressure had little effect on blistering formation, if any. While this does not prove that the explanations presented by Bras *et al.* and Malerba *et al*. are wrong, it shows that another mechanism for blister formation is responsible for the present results, compared to which the two mechanisms proposed are negligible. The nature of such mechanism was, at this point, still not clear. However, if the process was triggered during sulfurization, then one should, in principle, be able to gather clues and hints about the behavior of the system by significantly varying the sulfurization profiles. Therefore, a sequence of tests using both $\mathrm{Se}^{\mathrm{mid}}$ and $\mathrm{Se}^{\mathrm{top}}$ precursors was done for a wide range of sulfurization profiles, ranging from

very slow annealings, with R_+ as low as $0.1\ ℃/s$, to very fast ones, with R_+ up to $10\ ℃/s$. A graphical representation of the profiles used is provided in Fig. 5.11.

This approach proved to be very effective, as a clear tendency in the results appeared. It was observed that the heating rate R_+ was the most decisive factor: for slow heating rates – 0.2 and

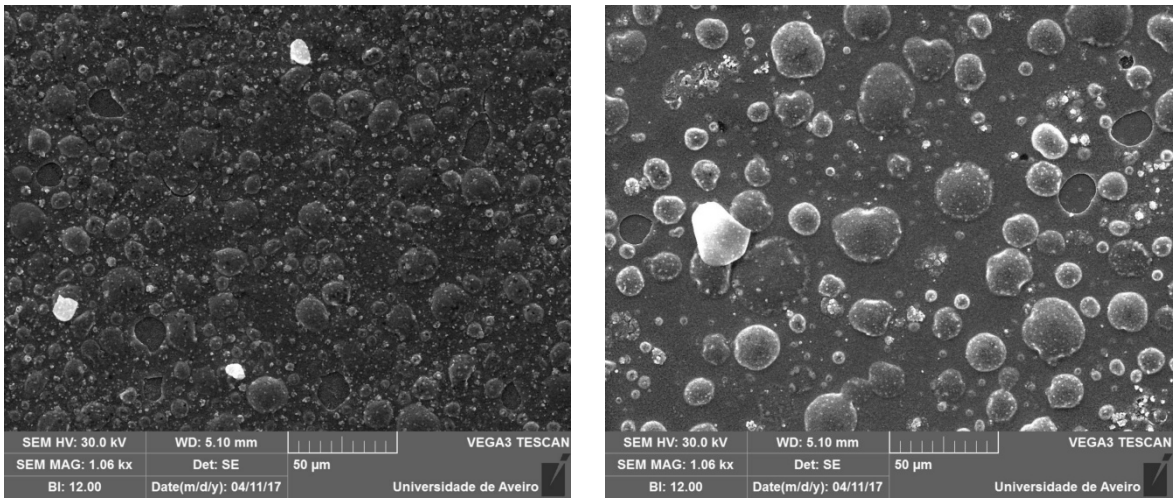

(a) (b)

Fig. 5.10 – Two absorbers resulting from Se^{top} precursors produced at the higher pressure of 6×10^{-3} mbar, (a) and (b) being the In and Out positions, respectively. The sulfurization conditions were $R_+ = 5\ ℃/s$, $T_P = 500\ ℃$, $\Delta t_P = 20$ min, $R_- = 0.2\ ℃/s$ to 300℃, followed by natural cooling. The absorbers have around 1% Se, and were not etched.

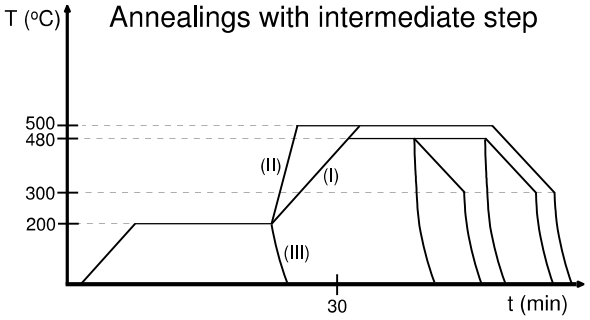

(a)

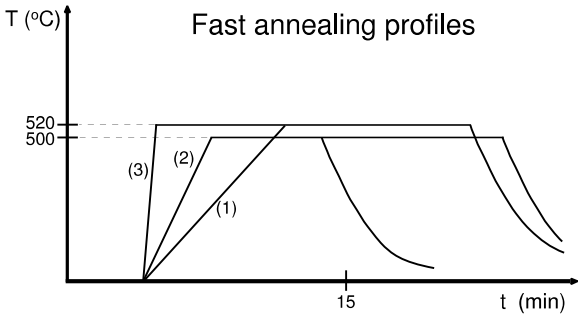

(b)

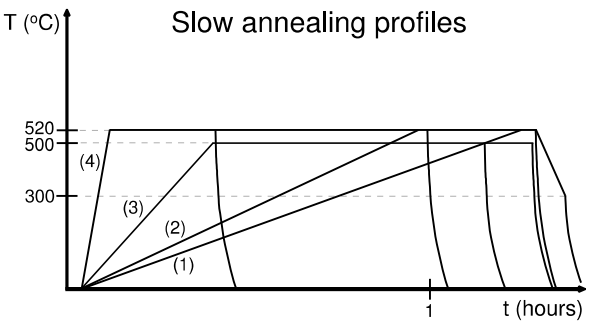

(c)

Fig. 5.11 – Different annealing profiles tested in this work. The sequences $R_{+1,2}(℃/s) \rightarrow T_{P1,2}(℃) \rightarrow \Delta t_{P1,2}(\text{min}) \rightarrow$ cooling are (NC – natural cooling):

$$\text{(a)}\begin{cases} 0.5 \rightarrow 200 \rightarrow 20' \rightarrow \begin{cases} (I)\ 0.5 \rightarrow \begin{cases} 500 \rightarrow \begin{cases} 10' \rightarrow -0.5 \rightarrow 300 \rightarrow NC \\ 20' \rightarrow -0.5 \rightarrow 300 \rightarrow NC \end{cases} \\ 480 \rightarrow 10' \rightarrow -0.5 \rightarrow 300 \rightarrow NC \end{cases} \\ (II)\ 1 \rightarrow 500 \rightarrow 20' \rightarrow -0.5 \rightarrow 300 \rightarrow NC \\ (III)\ NC \end{cases} \end{cases}$$

$$\text{(b)}\begin{cases} (1)\ 5 \rightarrow \begin{cases} 500 \rightarrow \begin{cases} 10' \rightarrow NC \\ 20' \rightarrow NC \end{cases} \\ 520 \rightarrow 20' \rightarrow NC \end{cases} \\ (2)\ 7 \rightarrow 30' \rightarrow NC \\ (3)\ 10 \rightarrow 30' \rightarrow NC \end{cases}$$

$$\text{(c)}\begin{cases} (1)\ 0.1 \rightarrow \begin{cases} 500 \rightarrow \begin{cases} 20' \rightarrow NC \\ 20' \rightarrow -0.2 \rightarrow 300 \rightarrow NC \end{cases} \\ 520 \rightarrow 20' \rightarrow NC \end{cases} \\ (2)\ 0.2 \rightarrow \begin{cases} 500 \rightarrow 20' \rightarrow NC \\ 520 \rightarrow \begin{cases} 1' \rightarrow NC \\ 20' \rightarrow NC \end{cases} \end{cases} \\ (3)\ 0.5 \rightarrow \begin{cases} 5' \rightarrow NC \\ 10' \rightarrow NC \end{cases} \\ (4)\ 1 \rightarrow 5' \rightarrow NC \end{cases}$$

$0.1\ ℃/s$ – and also for high eating rates – above $5℃/s$ – the size and/or density of blisters was visibly reduced. Some of the results are shown in Fig. 5.12. See, for instance, Fig. 5.12 (a), which can be directly compared with Fig. 5.2 (a), as the absorbers result from two halves of the same precursor. In some cases, blistering is almost completely suppressed, as in Fig. 5.12 (b), (c) and (d).

This is, however, still not enough to disprove the theories of Bras *et al.* and Malerba *et al.*. Such a behavior could, in principle, still be understood in the light of the models suggested by both groups – different heating rates can change the dynamics of the release of trapped Ar, and can also change the dynamics of the absorber growth, with possible change the mechanical stresses associated. Nevertheless, the results in the present work present new evidence, based on the heating rate,

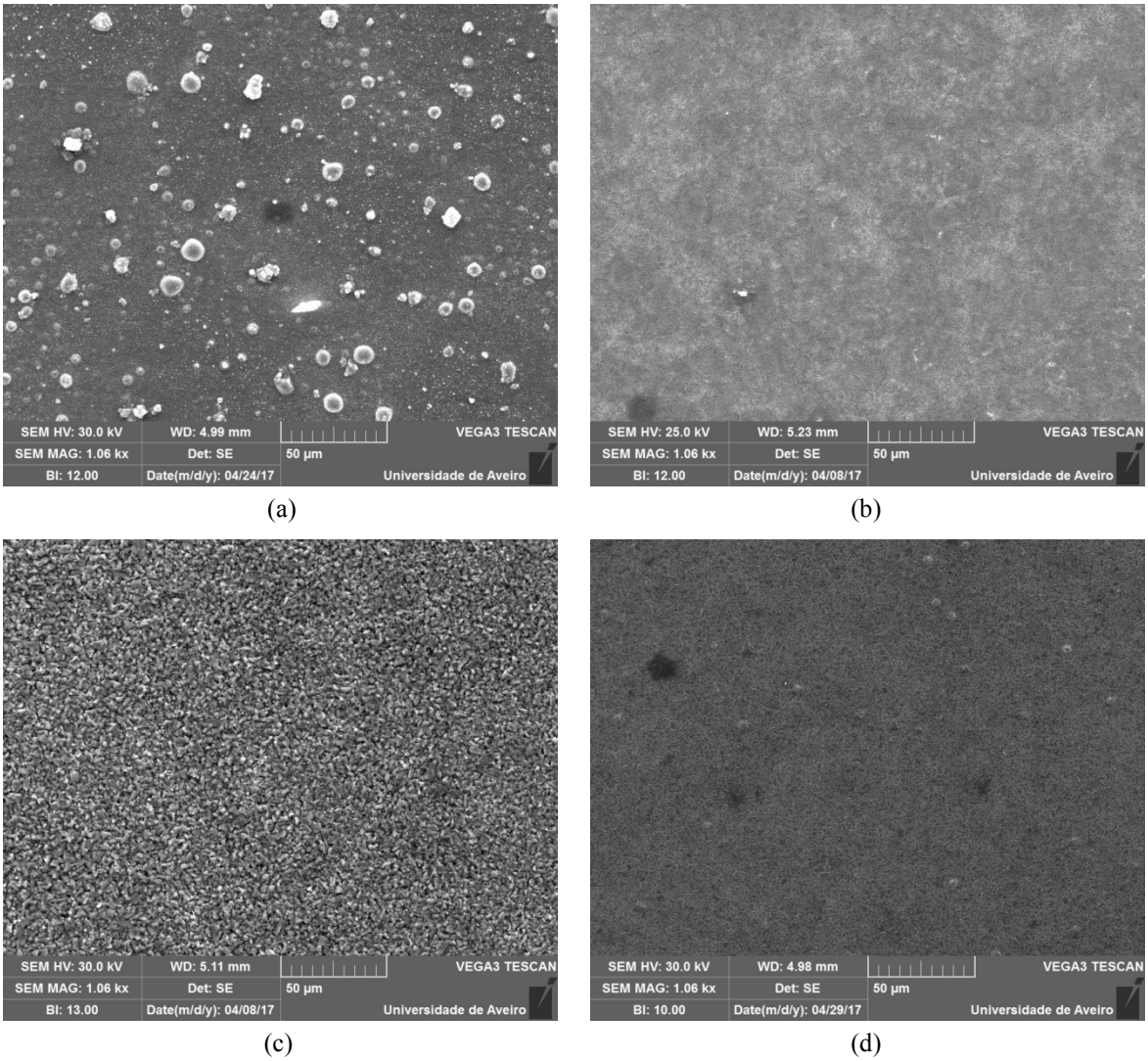

Fig. 5.12 – (a) An absorber produced using $0.2\ ℃/s \rightarrow 520℃ \rightarrow 1$ min → natural cooling. It compares directly with Fig. 5.2 (a), since different halves of the same precursor were used. Blisters still occur, but their size decreased significantly; (b) An absorber produced using $0.2\ ℃/s \rightarrow 500℃ \rightarrow 20$ min → natural cooling; (c) An absorber of the Down type produced using $0.1\ ℃/s \rightarrow 520℃ \rightarrow 20$ min → natural cooling; (d) An absorber produced using $7\ ℃/s \rightarrow 500℃ \rightarrow 30$ min → natural cooling. All these absorbers are non-etched and from Se^{mid} precursors – the Se^{top} also exhibited significant improvements in terms of blister reduction, but to a lesser extent than Se^{mid} precursors.

which was not considered by either group. Confronting these new results with each model would be an important step in clarifying the issue of blister formation in CZTS-based solar cells.

The question remains whether a third factor also exists, which could also explain the dynamics of blister formation observed in this work. One other explanation, based on reactant volatilization, was deemed plausible, and will be now discussed on qualitative grounds. It is well known that the low vapor pressures of SnS and SnSe can cause CZTSSe absorbers to decompose into their binary secondary phases, and elemental Sn can be lost due to volatilization of these compounds [9]. As these are also present in the precursors (see for example the Raman results of the present work, Fig. 5.3 (a)), losses by direct volatilization of precursors are also possible. Losses of over 80 % of the initial Sn quantity have been measured for vacuum annealing, as was shown for pure CZTS by Scragg *et al*. [77], who also showed that these losses can be controlled successfully when a minimum amount of elemental S (in that concrete study, but H_2S gas is also viable) and SnS are provided simultaneously. CZTS formation and reactant volatilization are thus naturally competing phenomena. One can understand this result in the light of basic principles, namely the Le Châtelier principle, as was done by Berg and Dale in [9] – S(e) and SnS(e) in excess need to be assured to shift the decomposition reaction towards the side with CZTS(e) as product. There are, in general, two different ways of achieving this: (i) Through conditions close to equilibrium, for example using sealed containers – such as a quartz tube. Then, the volume of SnS(e) lost is limited, being proportional to the volume of the container; (ii) Through non-equilibrium conditions where active measures are taken to bypass the decomposition reaction – these include annealing in an overpressurized atmosphere or compensating for the referred losses by actively supplying the compounds lost. This is possible for example using a partially sealed graphite box with added reactant powders. Significant improvements achieved by implementing these mechanisms have already been shown – see the discussion and references in [9].

The argument here constructed tries to suggest that reactant volatilization is directly linked to blister formation in CZTS, and that the two ideal heating rates – slow and high –, discovered in this work, partially achieve conditions (i) and (ii), respectively. Given that an RTP/A furnace with cooled walls was used in this work, annealing is always out of equilibrium regarding volatile species, because any evaporated mass will condense on the cooled walls – this condensation was clearly visible in the furnace used in this work after a large series of tests. However, by employing a very slow heating rate, the film is closer to thermal equilibrium, vertical thermal gradients are minimized, mass evaporation is slower and less violent, thus creating less blister-generating events. Thus, although evaporation losses can be large in total, the temporal (and thermal) spreading of the process uniformizes them and shifts the reaction dominance towards CZTSSe. This effect is emphasized in Se^{mid} precursors compared to Se^{top} precursors because excess Se is provided close to

each precursor layer, favoring absorber growth in depth, while evaporation losses are only visible near the surface. This could qualitatively explain the better results of Se^{mid} precursors and also why some smaller blisters and surface inhomogeneities are still visible in these, and why blisters which go through the whole film all the way to the Mo BC are hardly ever seen, in comparison to the earlier results described in the beginning of section 5. Another possibility exists, which is based on recent studies which show that CZTS compounds can be formed at low temperatures, as low as 260 ℃ [78], [79]. This formation temperature would be implicitly implicated in the slow thermal processing employed, further decreasing any evaporation losses directly from the precursors, which would then be limited only to possible surface decompositions of the absorber. As the heating rate is increased, these compromises are progressively lost, and blistering becomes dominant. Further increasing the heating rate then reaches the second limiting case of condition (ii). The precursors are quickly brought into temperatures above 500 ℃ where CZTS formation is dominant, and a few minutes are enough to form the absorber. The total amount of evaporation losses is lower and again limited to the surface of the absorbers. Interestingly, this possibly had been envisioned by Berg and Dale, who state that «Another kinetic approach not yet demonstrated in the literature would be to anneal for short times and to etch off any resulting secondary phases» [9]. The results in the present work suggest that this could be a possibility.

It is worth mentioning, also, that Bras *et al.* rejected the possibility of blistering being associated with the segregation and evaporation of volatile reactants, since no average composition change was detected in blisters [73]. But what if these composition changes are hard to detect? EDS is a detection method with a limited accuracy of measurement, and small mass variations can easily go unnoticed. To make matters worse, intrinsic element distribution variabilities from sample to sample or within different regions of a same sample can further mask these variations. Moreover, it could in principle occur that a significant part of volatile reactants trapped in bubbles do react to form CZTS, and only a small fraction is lost. This would be consistent with the findings in *Bras et al.*, corroborated in this work, that no composition changes can be detected in blisters. In this work, it was seen that unburst blisters have a grain size similar to homogenous regions, and exhibit the kesterite structure. The process of blister formation is thus a purely physical and morphological phenomenon. In fact, one could actually fit the model of entrapped Ar release proposed by *Bras et al.* to the volatilization of reactants in CZTS, since the same basic principles can apply. If this is true, then the dynamic changes due to different temperature profiles, discussed in the respective references of the mentioned work [73], could explain the results of the present work.

To gain further insight on the ideas discussed above, a series of new tests was conceptually planned and executed. In principle, specific changes in the precursor configuration should shift this competition between CZTS formation and reactant volatilization enough for it to have significant repercussions in blistering formation. Two such changes would be, for instance, changing the uppermost volatile SnS_2 precursor layer, or changing the number of precursor periods – in principle, a large number of periods (or ideally a co-sputtering configuration) would significantly improve the intermixing of elements and thus increase the speed of the reaction of CZTS formation, favoring it over reactant volatilization. Some preliminary tests were conducted, by fabricating precursors with 4 periods and 16 periods and removing the upper SnS_2 layer or switching its order with Se in Se^{top} precursors, but the results were not conclusive, and further tests should be conducted. Another test was conducted in order to try to achieve partially sealed atmosphere conditions. An improvised configuration using an inverted Petri dish on top of the graphite susceptor, covering the samples, was used. Additionally, SnS powders, with a total mass of 25.8 ± 0.1 mg were placed near the samples, on top of a glass substrate. Everything else remained as illustrated in Fig. 4.4. The first results were already positive, as annealing could be done at a rate of $R_+ = 1\ ℃/s$ without a critical occurrence of blisters. The advantages of higher heating rates is that the overall annealing process becomes faster, which has broad implications – for instance, the $Mo(S,Se)_2$ can be kept under control and is not increased unnecessarily and, in conjunction with the partially contained environment, total material losses can be minimized, as has been discussed, which improves the reproducibility of results. In particular, this battery of tests using the Petri dish and the rate of $R_+ = 1\ ℃/s$ achieved the production of absorbers with the highest Se content of all the absorbers produced in

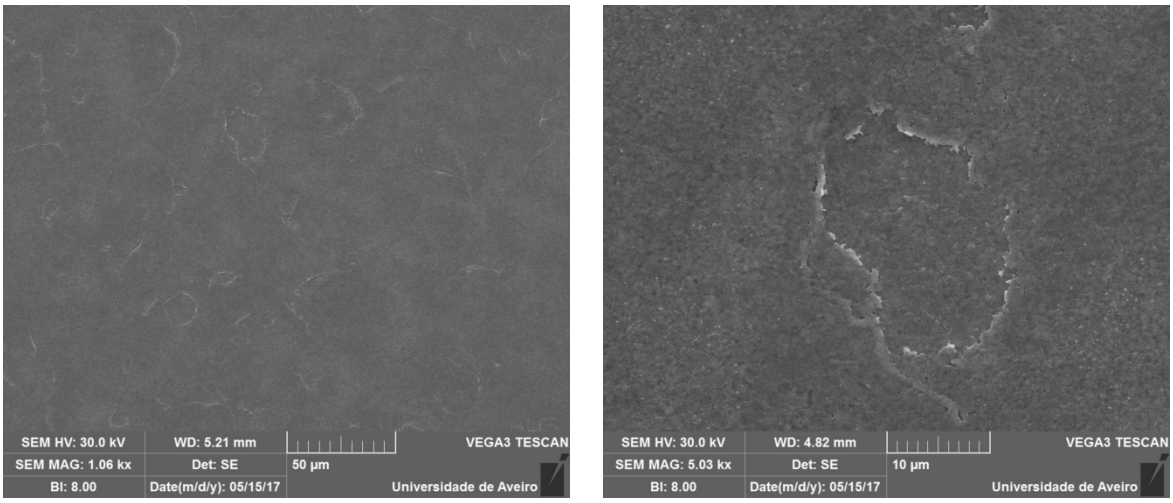

(a) (b)

Fig. 5.13 – SEM images of a non-etched absorber produced from standard Se^{mid} precursors in a Petri dish + SnS powder annealing using a sequence $1\ ℃/s \rightarrow 520\ ℃ \rightarrow 5$ min → natural cooling. In (a), some surface inhomogeneities are visible, and are shown in greater detail in (b). These appear to resemble blister craters, and seem to occur only superficially. The S/(S+Se) ratio was 0.85, the lowest among standard absorbers from any precursor type.

this work (except for the absorbers of the Down type), with a value of almost 6 %, corresponding to a $S/(S+Se)$ ratio of 0.85. The morphology of the absorber described here is shown in Fig. 5.13.

Surprisingly, despite these apparent improvements, no increase in photovoltaic efficiency could be demonstrated. In most cases, the devices exhibited rectifying behavior, but photovoltaic efficiency was very poor (below 0.1%). In some cases, the cells appeared to be completely short-circuited, despite having been thoroughly isolated using mechanical scribing. The results for the best cells are shown in Fig. 5.14 and Table 5.4. The device labeled "control" was an absorber fabricated in the same conditions as the champion device of Fig. 5.4, used as a reference. Notice how the thermal treatment improves the properties of the control sample, but in the case of sample P, performance is degraded after thermal treatment in the two best subcells. It will serve merely as an empirical observation, as no explanation can be provided at this point.

The information available is not enough to understand why these devices are severely underperforming despite the significant improvements in terms of blister formation. One could speculate that some fabrication problems are present in some of the stages of production, based on the fact that the control sample could not reproduce the results of the champion device. Its V_{oc} value of 413 mV is typical of cells with efficiency over 1%, but its J_{sc} and FF are very low, much lower compared to the first devices produced, as shown in Table 5.3. Additionally, since efficiencies are so low, and no particular precursor configuration stood out, nothing can be concluded regarding the

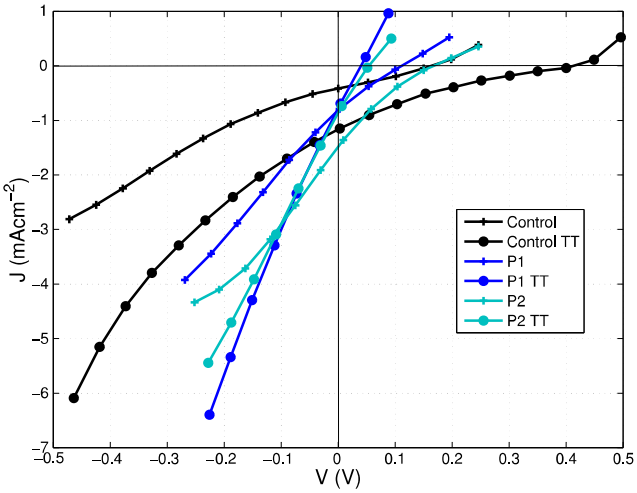

Table 5.4 – Device parameters for the the best devices that resulted from the blister elimination tests, before and after post-fabrication thermal treatment (TT).

	V_{oc} (mV)	J_{sc} (mA/cm^2)	FF (%)	η (%)
Control	164	0.41	28.6	0.02
Control TT	413	1.17	16.4	0.08
P1	112	0.81	22.0	0.02
P1 TT	39	0.77	8.9	0.00
P2	168	1.49	18.3	0.05
P2 TT	53	0.86	9.8	0.00

Fig. 5.14 – Light IV curves for some of the devices which exhibited less blistering. The "control" sample was an absorber fabricated in the same conditions as the champion device (see Fig. 5.4). The sample labeled "P", measured in two different subcells P1 and P2 was made from Se^{top} precursors using a 16 period configuration where the upper SnS_2 layer was removed. Both absorbers were etched with KCN.

utility of changing that configuration, as was mentioned in the discussion above.

Some of the absorbers produced in this work were also analyzed using rf-PGD-TOFMS. The configurations analyzed consisted in three different types of absorber (all non-etched): (i) one with $S/(S+Se) = 0.99$, from Se^{mid} precursors sulfurized using an intermediate step, with severe blistering; (ii) one with $S/(S+Se) = 0.97$, from Se^{mid} precursors sulfurized using a slow heating rate, with a low occurrence of blisters; (iii) one absorber of the Down type, with $S/(S+Se) = 0.71$, sulfurized in the same conditions as (ii) but using Se^{top} precursors, also with low blistering phenomena. Results are shown in Fig. 5.15.

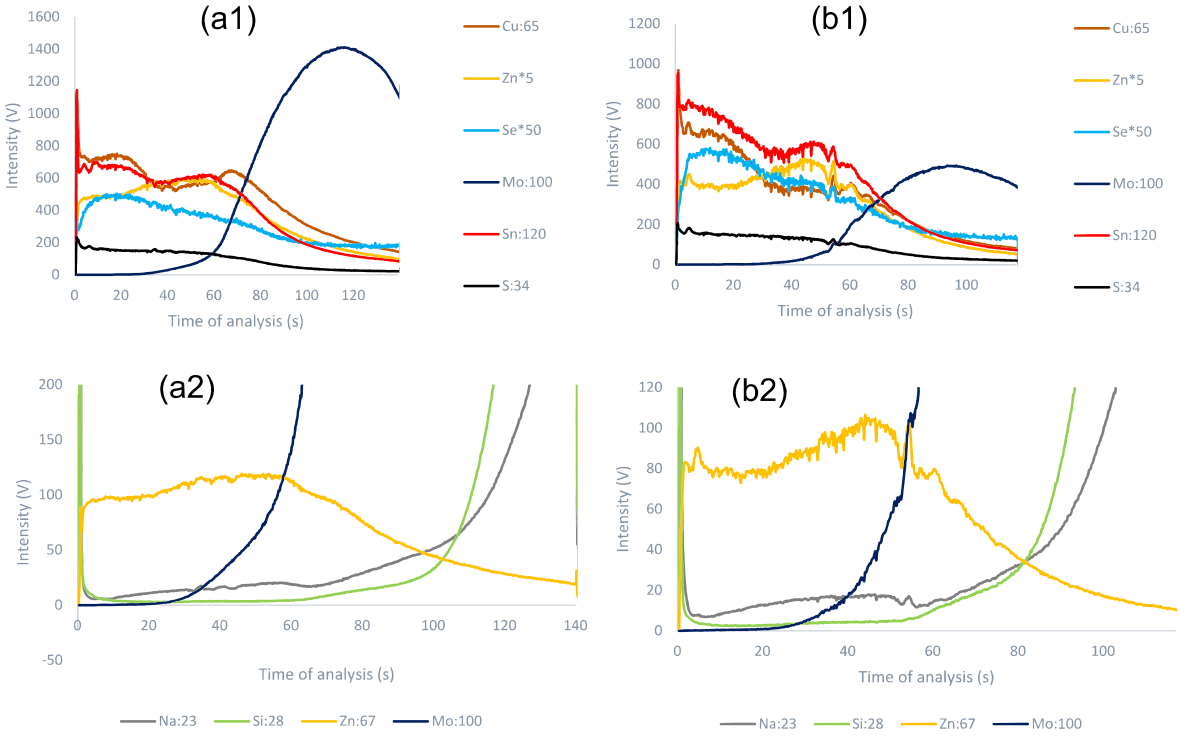

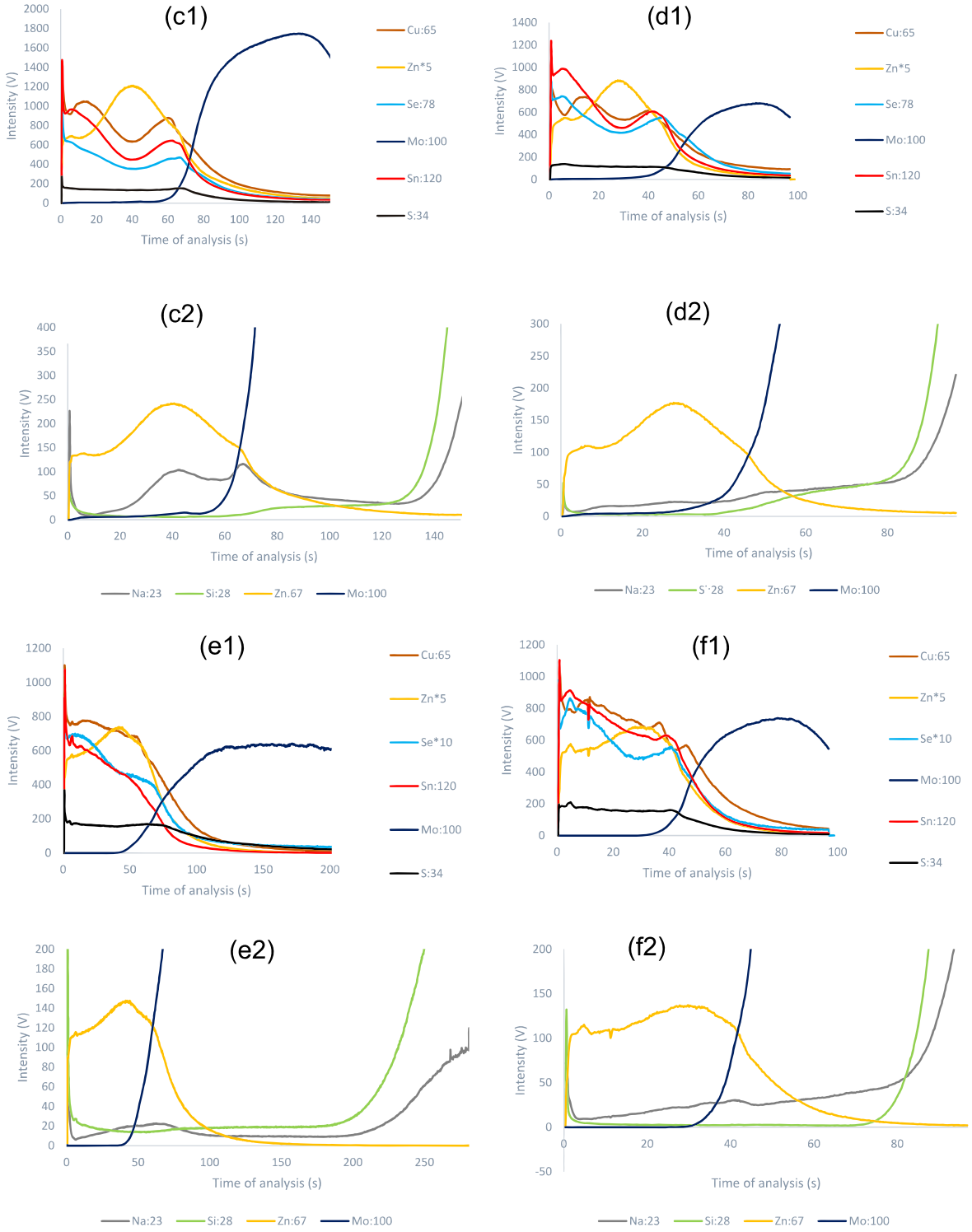

Fig. 5.15 – Results of rf-PGD-TOFMS. Two measurements per sample are presented. Using the convention set forth in the main text, (a) and (b) correspond to sample (i), (c) and (d) to sample (ii) and (f) and (e) to sample (iii) These measurements were courtesy of a research group part of the Physical and Analytical Chemistry Department of the Faculty of Chemistry of the University of Oviedo, in Spain.

The results reveal some new insights on the samples. In terms of the metal profiles, it can be seen that Cu and Sn exhibit a similar evolution along the thickness of the absorbers, unlike Zn,

which has a different distribution trend. This qualitatively indicates that the composition ratios are not uniform along the thickness of the absorber, which could lead to the segregation of secondary phases and to a high concentration of defects detrimental to photovoltaic performance. This trend is seen in all samples, indicating that this could be a fundamental reason for the low photovoltaic performance exhibited by the absorbers produced in this work. In contrast to the metal elements, the S profile is nearly constant. It can also be seen that some Na diffuses from the glass substrate through the Mo into the absorbers. This has a plethora of positive effects, as has been briefly described in section 3.1. Another important feature of Fig. 5.15 is the Se profiles. It can be seen that the Se profiles are more constant in (a,b) and (c,d), which correspond to Se^{mid} precursors, compared to (e,f), where the precursor was Se^{top}. This was intuitively expected given the uniform distribution of the elemental Se in the precursor layers. It would be an interesting test to change the Se in the Se^{mid} precursors, for example including thicker layers towards the surface, and testing the resulting profiles. The Se profiles of (e1) and (f1) show that Se^{top} precursors are a viable way of introducing a $S/(S + Se)$ gradient in depth, and have a distribution similar to the original *ansatz* used in section 3.2.2 – notice how in (a1), (b1), (e1) and (f1) the surface seems depleted of Se, as had been originally predicted, based on superficial resubstitution of Se for S. It would be interesting to analyze the Se profile in greater detail in future measurements, as it also appears that in the case of (e1), the Se distribution resembles more an error function than a gaussian function, which could be indicative that Se diffusion from Se^{top} precursors follows infinite dopant reservoir model [50, Ch. 7], indicating that the Se layer deposited on the top is very thick. There is, however, an apparent notch in Se profiles close to the middle of the absorbers. This type of notch is detrimental for photovoltaic performance when it occurs far from the surface, as has been discussed in 3.2.2. A similar notch is seen also for the metal elements. The reason for this behavior is not known.

Another fact worth of mentioning is that in (a,b) there seems to be a higher Se depletion near the surface. Given that this sample had a higher occurrence of blisters, this can be an indicator linked to that fact – it could possibly result from SnSe volatilization. The Sn signal would still be relatively unaffected, as is the case, since its amount is much larger than the total amount of Se.

6. Concluding remarks and future work

CZTS based compounds are less stable than their CIGS counterparts, which means that their production methods should be very rigorous and specific in order to optimize their properties. An example of this general problem has been seen throughout this work for the case of blister formation. It was demonstrated that blister formation can be significantly changed just by adjusting the annealing profile, which is an effect that has not been discussed in current literature. Another example was the need to etch the samples in order to remove $Cu_{2-x}S$ phases which were systemati-

cally detected. A solar cell with a maximum efficiency of 1.3% could be produced despite the occurrence of burst blisters, hinting that there is room for performance improvement using the methods implemented. However, no performance improvements could be demonstrated when blisters where controlled, which could not be understood. Thus, it is essential to fabricate a higher number of devices replicating these conditions, to get more statistical significance and notions of process reproducibility. If this reproducibility is achieved, the work can be focused on each specific layer of the device. Otherwise, more emphasis should be placed on experimental configurations and procedures to ensure uniformization.

In terms of the absorber layer, there are many pertinent characterization tests that could be implemented. For instance, Raman analysis along the thickness of the cell could provide more insights on the phases present in depth and complement the results of the rf-PGD-TOFMS. In addition, considering the poor diode behavior of the devices produced, the pn junctions fabricated should be assessed in detail. One important measurement here would be to study the influence of experimental conditions on the carrier concentration of CZTS and CdS, in order to find a way to achieve one-sided n+p junctions. Achieving this in practice turns out to be very difficult, which is a small detail that seems to be overlooked by many researchers (see discussion in [45]). Additionally, new work could be conducted in terms of the possibility of forming CZTS through low temperature annealing, an approach which has been discovered recently and has produced state-of-the-art results already [78], [79].

In terms of bandgap grading, the true bandgap profile was never actually measured in the present work, and was implicitly assumed based on the relationship of Eq. (10). Naturally, this is not sufficient, and the actual bandgap variations with depth should be measured directly. There are some ways to do this, and these methods have already been developed and applied to CIGS. See for example references [80], [81].

References

[1] VDMA, "International Technology Roadmap for Photovoltaic (ITRPV): 2016 Results," 2017.

[2] M. Schmela, G. Masson, and N. N. T. Mai, "Global Market Outlook for Solar Power / 2016 - 2020," 2016.

[3] L. Partain, R. Hansen, S. Hansen, D. Bennett, A. Newlands, and L. Fraas, "'Swanson's Law' plan to mitigate global climate change," in *2016 IEEE 43rd Photovoltaic Specialists Conference (PVSC)*, 2016, vol. 2014, pp. 3335–3340.

[4] V. Shah and J. Booream-Phelps, "Crossing the Chasm. Solar Grid Parity in a Low Oil Price Era," 2015.

[5] P. Sanders, "Chile Energy Auction Gives Bachelet a Success to Boast About," *Bloomberg*, 2016.

[6] OMIE, "Price Report 2016," 2017.

[7] *Diretiva n.º 1/2017 da Entidade Reguladora dos Serviços Energéticos*. Diário da República, 2ª Série - N.º 2, 2017.

[8] M. Woodhouse, R. Jones-Albertus, D. Feldman, R. Fu, K. Horowitz, D. Chung, D. Jordan, and S. Kurtz, "On the Path to SunShot : The Role of Advancements in Solar Photovoltaic Efficiency , Reliability , and Costs," no. 2016, p. 44, 2016.

[9] K. Ito, *Copper Zinc Tin Sulfide-Based Thin Film Solar Cells*. John Wiley & Sons, Ltd, 2015.
[10] *Directive 2008/98/EC of the European Parliament and of the Council of 19 November 2008 on waste and repealing certain directives*. Official Journal of the Europian Union, 2008.
[11] S. R. Taylor and S. M. McClennan, *The Continental Crust: Its Composition and Evolution: An Examination of the Geochemical Record Preserved in Sedimentary Rocks*. Blackwell Scientific Publications, 1985.
[12] B. A. Andersson, "Materials availability for large-scale thin-film photovoltaics," *Prog. Photovoltaics Res. Appl.*, vol. 8, no. 1, pp. 61–76, Feb. 2000.
[13] C. S. Tao, J. Jiang, and M. Tao, "Natural resource limitations to terawatt-scale solar cells," *Sol. Energy Mater. Sol. Cells*, vol. 95, no. 12, pp. 3176–3180, 2011.
[14] M. Kumar, A. Dubey, N. Adhikari, S. Venkatesan, and Q. Qiao, "Strategic review of secondary phases, defects and defect-complexes in kesterite CZTS–Se solar cells," *Energy Environ. Sci.*, vol. 8, no. 11, pp. 3134–3159, 2015.
[15] T. D. Lee and A. U. Ebong, "A review of thin film solar cell technologies and challenges," *Renew. Sustain. Energy Rev.*, vol. 70, no. September 2015, pp. 1286–1297, Apr. 2017.
[16] W. Wang, M. T. Winkler, O. Gunawan, T. Gokmen, T. K. Todorov, Y. Zhu, and D. B. Mitzi, "Device characteristics of CZTSSe thin-film solar cells with 12.6% efficiency," *Adv. Energy Mater.*, vol. 4, no. 7, pp. 1–5, 2014.
[17] K.-J. Yang, D.-H. Son, S.-J. Sung, J.-H. Sim, Y.-I. Kim, S.-N. Park, D.-H. Jeon, J. Kim, D.-K. Hwang, C.-W. Jeon, D. Nam, H. Cheong, J.-K. Kang, and D.-H. Kim, "A Band-Gap-Graded CZTSSe Solar Cell with 12.3% Efficiency," *J. Mater. Chem. A*, vol. 4, no. 26, pp. 10151–10158, 2016.
[18] X. Liu, Y. Feng, H. Cui, F. Liu, X. Hao, G. Conibeer, D. B. Mitzi, and M. Green, "The current status and future prospects of kesterite solar cells: a brief review," *Prog. Photovolt Res. Appl.*, vol. 24, pp. 879–898, 2016.
[19] T. Gershon, T. Gokmen, O. Gunawan, R. Haight, S. Guha, and B. Shin, "Understanding the relationship between $Cu_2ZnSn(S,Se)_4$ material properties and device performance," *MRS Commun.*, vol. 4, no. 4, pp. 159–170, Dec. 2014.
[20] M. Burgelman, K. Decock, A. Niemegeers, J. Verschraegen, and S. Degrave, "SCAPS manual Version 29 december 2016." 2016.
[21] S. Adachi, *Earth-Abundant Materials for Solar Cells: Cu2-II-IV-VI4 Semiconductors*. John Wiley & Sons, Ltd, 2015.
[22] S. Das, K. C. Mandal, and R. N. Bhattacharya, "Earth-Abundant $Cu_2ZnSn(S,Se)_4$ (CZTSSe) Solar Cells," in *Semiconductor Materials for Solar Photovoltaic Cells*, vol. 218, M. P. Paranthaman, W. Wong-Ng, and R. N. Bhattacharya, Eds. Cham: Springer International Publishing, 2016, pp. 25–74.
[23] A. Janotti and C. G. Van de Walle, "Fundamentals of zinc oxide as a semiconductor," *Rep Prog Phy*, vol. 72, no. 12, p. 126501, Dec. 2009.
[24] A. E. Delahoy and S. Guo, "Transparent Conducting Oxides for Photovoltaics," in *Handbook of Photovoltaic Science and Engineering*, John Wiley & Sons, Ltd, 2011, pp. 716–796.
[25] H. Liu, V. Avrutin, N. Izyumskaya, Ü. Özgr, H. Morkoç, Ü. Özgür, H. Morkoç, Ü. Özgr, and H. Morkoç, "Transparent conducting oxides for electrode applications in light emitting and absorbing devices," *Superlattices Microstruct.*, vol. 48, no. 5, pp. 458–484, Nov. 2010.
[26] A. Chirilă, S. Buecheler, F. Pianezzi, P. Bloesch, C. Gretener, A. R. Uhl, C. Fella, L. Kranz, J. Perrenoud, S. Seyrling, R. Verma, S. Nishiwaki, Y. E. Romanyuk, G. Bilger, and A. N. Tiwari, "Highly efficient $Cu(In,Ga)Se_2$ solar cells grown on flexible polymer films.," *Nat. Mater.*, vol. 10, no. 11, pp. 857–861, 2011.
[27] P. Würfel and U. Würfel, *Physics of Solar Cells: From Basic Principles To Advanced Concepts*, 3rd ed. Wiley-VCH, 2016.
[28] A. Mule, B. Vermang, M. Sylvester, G. Brammertz, S. Ranjbar, T. Schnabel, N. Gampa, M. Meuris, and J. Poortmans, "Effect of different alkali (Li, Na, K, Rb, Cs) metals on $Cu_2ZnSnSe_4$ solar cells," *Thin Solid Films*, Nov. 2016.
[29] W. Li, X. Yan, A. G. Aberle, and S. Venkataraj, "Effect of deposition pressure on the properties of magnetron-sputter-deposited molybdenum back contacts for CIGS solar cells," *Jpn. J. Appl. Phys.*, vol. 54, Aug. 2015.
[30] M. Bär, S. Nishiwaki, L. Weinhardt, S. Pookpanratana, W. N. Shafarman, and C. Heske, "Electronic level alignment at the deeply buried absorber/Mo interface in chalcopyrite-based thin film solar cells," *Appl. Phys. Lett.*, vol. 93, no. 4, p. 42110, Jul. 2008.
[31] J. J. Scragg, J. T. Wätjen, M. Edoff, T. Ericson, T. Kubart, and C. Platzer-Björkman, "A Detrimental

Reaction at the Molybdenum Back Contact in Cu_2 $ZnSn(S,Se)_4$ Thin-Film Solar Cells," *J. Am. Chem. Soc.*, vol. 134, no. 47, pp. 19330–19333, Nov. 2012.
[32] P. D. Antunez, D. M. Bishop, Y. S. Lee, T. Gokmen, O. Gunawan, T. S. Gershon, T. K. Todorov, S. Singh, and R. Haight, "Back Contact Engineering for Increased Performance in Kesterite Solar Cells," *Adv. Energy Mater.*, vol. 1602585, p. 1602585, Apr. 2017.
[33] Y. S. Lee, T. Gershon, O. Gunawan, T. K. Todorov, T. Gokmen, Y. Virgus, and S. Guha, "$Cu_2ZnSnSe_4$ thin-film solar cells by thermal co-evaporation with 11.6% efficiency and improved minority carrier diffusion length," *Adv. Energy Mater.*, vol. 5, no. 7, pp. 2–5, 2015.
[34] S. Bourdais, C. Choné, B. Delatouche, A. Jacob, G. Larramona, C. Moisan, A. Lafond, F. Donatini, G. Rey, S. Siebentritt, A. Walsh, and G. Dennler, "Is the Cu/Zn Disorder the Main Culprit for the Voltage Deficit in Kesterite Solar Cells?," *Adv. Energy Mater.*, vol. 6, no. 12, p. 1502276, Jun. 2016.
[35] A. Redinger, D. M. Berg, P. J. Dale, and S. Siebentritt, "The consequences of kesterite equilibria for efficient solar cells," *J. Am. Chem. Soc.*, vol. 133, no. 10, pp. 3320–3323, Mar. 2011.
[36] C.-H. H. Cai, S.-Y. Y. Wei, W.-C. C. Huang, J. Lin, T.-H. H. Yeh, and C.-H. H. Lai, "Efficiency enhancement by adding SnS powder during selenization for $Cu_2ZnSn(S,Se)_4$ thin film solar cells," *Sol. Energy Mater. Sol. Cells*, vol. 145, pp. 296–302, Feb. 2016.
[37] O. Gunawan, T. Gokmen, and D. B. Mitzi, "Suns - Voc characteristics of high performance kesterite solar cells," *J. Appl. Phys.*, vol. 116, no. 8, p. 84504, Aug. 2014.
[38] T. P. Dhakal, S. Harvey, M. van Hest, and G. Teeter, "Back contact band offset study of Mo-CZTS based solar cell structure by using XPS/UPS techniques," in *2015 IEEE 42nd Photovoltaic Specialist Conference (PVSC)*, 2015, pp. 1–4.
[39] J. Bardeen, "Surface States and Rectification at a Metal Semi-Conductor Contact," *Phys. Rev.*, vol. 71, no. 10, pp. 717–727, May 1947.
[40] S. M. Sze and K. K. NG, *Physics of Semiconductor Devices*, 3rd ed. Wiley-Interscience, 2007.
[41] D. R. Lide, *CRC Handbook of Chemistry and Physics, 85th Edition*. Taylor & Francis, 2004.
[42] W. Shockley and H. J. Queisser, "Detailed Balance Limit of Efficiency of p-n Junction Solar Cells," *J. Appl. Phys.*, vol. 32, no. 3, pp. 510–519, Mar. 1961.
[43] R. T. Tung, "The physics and chemistry of the Schottky barrier height," *Appl. Phys. Rev.*, vol. 1, no. 1, p. 11304, Mar. 2014.
[44] S. Chen, A. Walsh, X.-G. Gong, and S.-H. Wei, "Classification of Lattice Defects in the Kesterite Cu_2ZnSnS_4 and $Cu_2ZnSnSe_4$ Earth-Abundant Solar Cell Absorbers," *Adv. Mater.*, vol. 25, no. 11, pp. 1522–1539, Mar. 2013.
[45] A. D. Collord, H. Xin, and H. W. Hillhouse, "Combinatorial Exploration of the Effects of Intrinsic and Extrinsic Defects in $Cu_2ZnSn(S,Se)_4$," *IEEE J. Photovoltaics*, vol. 5, no. 1, pp. 288–298, Jan. 2015.
[46] I. D. Olekseyuk, I. V. Dudchak, and L. V. Piskach, "Phase equilibria in the Cu_2S–ZnS–SnS_2 system," *J. Alloys Compd.*, vol. 368, no. 1–2, pp. 135–143, Apr. 2004.
[47] S. Schorr, "The crystal structure of kesterite type compounds: A neutron and X-ray diffraction study," *Sol. Energy Mater. Sol. Cells*, vol. 95, no. 6, pp. 1482–1488, Jun. 2011.
[48] S. R. Kodigala, *$Cu(In_{1-x}Ga_x)Se_2$ Based Thin Film Solar Cells*. Elsevier Science, 2011.
[49] A. Walsh, S. Chen, S. H. Wei, and X. G. Gong, "Kesterite thin-film solar cells: Advances in materials modelling of Cu_2ZnSnS_4," *Adv. Energy Mater.*, vol. 2, no. 4, pp. 400–409, 2012.
[50] E. F. Schubert, *Doping in III-V Semiconductors:* Author, 2015.
[51] J. B. Varley and V. Lordi, "Electrical properties of point defects in CdS and ZnS," *Appl. Phys. Lett.*, vol. 103, no. 10, p. 102103, Sep. 2013.
[52] A. Crovetto, M. L. N. Palsgaard, T. Gunst, T. Markussen, K. Stokbro, M. Brandbyge, and O. Hansen, "Interface band gap narrowing behind open circuit voltage losses in Cu2ZnSnS4 solar cells," *Appl. Phys. Lett.*, vol. 83903, no. 8, p. 83903, Feb. 2017.
[53] K. Decock, J. Lauwaert, and M. Burgelman, "Characterization of graded CIGS solar cells," *Energy Procedia*, vol. 2, no. 1, pp. 49–54, Aug. 2010.
[54] T. Gokmen, O. Gunawan, T. K. Todorov, and D. B. Mitzi, "Band tailing and efficiency limitation in kesterite solar cells," *Appl. Phys. Lett.*, vol. 103, no. 10, p. 103506, Sep. 2013.
[55] M. Courel, F. A. Pulgarín-Agudelo, J. A. Andrade-Arvizu, and O. Vigil-Galán, "Open-circuit voltage enhancement in CdS/$Cu_2ZnSnSe_4$-based thin film solar cells: A metal–insulator–semiconductor (MIS) performance," *Sol. Energy Mater. Sol. Cells*, vol. 149, pp. 204–212, May 2016.
[56] S. Siebentritt, "Why are kesterite solar cells not 20% efficient?," *Thin Solid Films*, vol. 535, no. 1, pp. 1–4, May 2013.
[57] C. Platzer-Björkman, C. Frisk, J. K. Larsen, T. Ericson, S.-Y. Li, J. J. S. Scragg, J. Keller, F. Larsson,

and T. Törndahl, “Reduced interface recombination in Cu 2 ZnSnS 4 solar cells with atomic layer deposition Zn 1− x Sn x O y buffer layers,” *Appl. Phys. Lett.*, vol. 107, no. 24, p. 243904, Dec. 2015.
[58] C. Yan, F. Liu, K. Sun, N. Song, J. A. Stride, F. Zhou, X. Hao, and M. Green, “Boosting the efficiency of pure sulfide CZTS solar cells using the In/Cd-based hybrid buffers,” *Sol. Energy Mater. Sol. Cells*, vol. 144, pp. 700–706, Jan. 2016.
[59] H. Lüth, *Surfaces and Interfaces of Solids*, 2nd ed. Springer Berlin Heidelberg, 1993.
[60] T. Ashrafee, K. Aryal, G. Rajan, S. Karki, V. Ranjan, A. Rockett, R. W. Collins, O. Ayala, and S. Marsillac, “Effect of substrate temperature on sputtered molybdenum film as a back contact for Cu(In,Ga)Se_2 solar cells,” in *2015 IEEE 42nd Photovoltaic Specialist Conference (PVSC)*, 2015, pp. 1–5.
[61] P. A. Fernandes, P. M. P. Salomé, and A. F. da Cunha, “Precursors’ order effect on the properties of sulfurized Cu 2 ZnSnS 4 thin films,” *Semicond. Sci. Technol.*, vol. 24, no. 10, p. 105013, 2009.
[62] G. L. Weissler and R. W. Carlson, *Vacuum Physics and Technology*. Elsevier Science, 1980.
[63] “Hydrogen Sulfide Safety Data Sheet.” Airgas, 2017.
[64] H. Khallaf, I. O. Oladeji, G. Chai, and L. Chow, “Characterization of CdS thin films grown by chemical bath deposition using four different cadmium sources,” *Thin Solid Films*, vol. 516, no. 21, pp. 7306–7312, Sep. 2008.
[65] J. K. Larsen, Y. Ren, N. Ross, E. Särhammar, S.-Y. Li, and C. Platzer-Björkman, “Surface modification through air annealing $Cu_2ZnSn(S,Se)_4$ absorbers,” *Thin Solid Films*, pp. 8–11, Aug. 2016.
[66] J. I. Goldstein, D. E. Newbury, P. Echlin, D. C. Joy, C. E. Lyman, E. Lifshin, L. Sawyer, and J. R. Michael, *Scanning Electron Microscopy and X-ray Microanalysis*, 3rd ed. Springer US, 2003.
[67] P. A. Fernandes, P. M. P. Salomé, and A. F. da Cunha, “Growth and Raman scattering characterization of Cu_2ZnSnS_4 thin films,” *Thin Solid Films*, vol. 517, no. 7, pp. 2519–2523, Feb. 2009.
[68] P. M. P. Salomé, J. Malaquias, P. A. Fernandes, M. S. Ferreira, A. F. da Cunha, J. P. Leitão, J. C. Gonzalez, and F. M. Matinaga, “Growth and characterization of Cu2ZnSn(S,Se)4 thin films for solar cells,” *Sol. Energy Mater. Sol. Cells*, vol. 101, pp. 147–153, Jun. 2012.
[69] D. B. Mitzi, O. Gunawan, T. K. Todorov, K. Wang, and S. Guha, “The path towards a high-performance solution-processed kesterite solar cell,” *Sol. Energy Mater. Sol. Cells*, vol. 95, no. 6, pp. 1421–1436, Jun. 2011.
[70] J. He, L. Sun, S. Chen, Y. Chen, P. Yang, and J. Chu, “Composition dependence of structure and optical properties of $Cu_2ZnSn(S,Se)_4$ solid solutions: An experimental study,” *J. Alloys Compd.*, vol. 511, no. 1, pp. 129–132, 2012.
[71] M. Grossberg, J. Krustok, J. Raudoja, K. Timmo, M. Altosaar, and T. Raadik, “Photoluminescence and Raman study of $Cu_2ZnSn(Se_xS_{1-x})_4$ monograins for photovoltaic applications,” *Thin Solid Films*, vol. 519, no. 21, pp. 7403–7406, Aug. 2011.
[72] C. Malerba, M. Valentini, C. L. L. Azanza Ricardo, A. Rinaldi, E. Cappelletto, P. Scardi, and A. Mittiga, “Blistering in Cu_2ZnSnS_4 thin films: correlation with residual stresses,” *Mater. Des.*, vol. 108, pp. 725–735, Oct. 2016.
[73] P. Bras, J. Sterner, and C. Platzer-Björkman, “Investigation of blister formation in sputtered Cu_2ZnSnS_4 absorbers for thin film solar cells,” *J. Vac. Sci. Technol. A Vacuum, Surfaces, Film.*, vol. 33, no. 6, p. 61201, Nov. 2015.
[74] H. Katagiri, K. Jimbo, W. S. Maw, K. Oishi, M. Yamazaki, H. Araki, and A. Takeuchi, “Development of CZTS-based thin film solar cells,” *Thin Solid Films*, vol. 517, no. 7, pp. 2455–2460, Feb. 2009.
[75] A. Thompson, D. Attwood, E. Gullikson, M. Howells, K.-J. Kim, J. Kirz, J. Kortright, I. Lindau, Y. Liu, P. Pianetta, A. Robinson, J. Scofield, J. Underwood, G. Williams, and H. Winick, *X-Ray Data Booklet*, 3rd ed. Lawrence Berkeley National Laboratory, University of California, 2009.
[76] H. Windischmann, “Intrinsic stress in sputter-deposited thin films,” *Crit. Rev. Solid State Mater. Sci.*, vol. 17, no. 6, pp. 547–596, 1992.
[77] J. J. Scragg, T. Ericson, T. Kubart, M. Edoff, and C. Platzer-Björkman, “Chemical Insights into the Instability of Cu2ZnSnS4 Films during Annealing,” *Chem. Mater.*, vol. 23, no. 20, pp. 4625–4633, Oct. 2011.
[78] Y. Feng, T.-K. Lau, G. Cheng, L. Yin, Z. Li, H. Luo, Z. Liu, X. Lu, C. Yang, and X. Xiao, “A low-temperature formation path toward highly efficient Se-free Cu_2ZnSnS_4 solar cells fabricated through sputtering and sulfurization,” *CrystEngComm*, vol. 18, no. 6, pp. 1070–1077, 2016.
[79] J. H. Lee, H. J. Choi, W. M. Kim, J. H. Jeong, and J. K. Park, “Effect of pre-annealing on the phase

formation and efficiency of CZTS solar cell prepared by sulfurization of Zn/(Cu,Sn) precursor with H_2S gas," *Sol. Energy*, vol. 136, pp. 499–504, Oct. 2016.

[80] M. Bär, S. Nishiwaki, L. Weinhardt, S. Pookpanratana, O. Fuchs, M. Blum, W. Yang, J. D. Denlinger, W. N. Shafarman, and C. Heske, "Depth-resolved band gap in $Cu(In,Ga)(S,Se)_2$ thin films," *Appl. Phys. Lett.*, vol. 93, no. 24, p. 244103, Dec. 2008.

[81] M. P. Heinrich, Z.-H. Zhang, Y. Zhang, O. Kiowski, M. Powalla, U. Lemmer, and A. Slobodskyy, "Direct measurements of band gap grading in polycrystalline CIGS solar cells," Sep. 2010.

[82] N. E. Gorji, M. D. Perez, U. Reggiani, and L. Sandrolini, "A New Approach to Valence and Conduction Band Grading in CIGS Thin Film Solar Cells," *Int. J. Eng. Technol.*, vol. 4, no. 5, pp. 573–576, 2012.